applied sciences

MDPI

Article

Dynamic Modeling, Dynamic Characteristics, and Slight Self-Guidance Ability at High Speeds of Independently Rotating Wheelset for Railway Vehicles

Xingheng Jia [1], Yuming Yin [2] and Wenjun Wang [1,*]

[1] School of Vehicle and Mobility, Tsinghua University, Beijing 100084, China; jiaxhstar@163.com
[2] College of Mechanical Engineering, Zhejiang University of Technology, Hangzhou 310023, China; yinyuming@zjut.edu.cn
* Correspondence: wj_wang@mail.tsinghua.edu.cn

Featured Application: The technology of the independently rotating wheelset has the potential to be introduced into urban rail transit to improve small-radius curve negotiation performance. In-depth knowledge on the dynamics of the independently rotating wheelset prompts better bogie structure design and stimulates further applied research.

Abstract: For better small-radius curve negotiation performance, the independently rotating wheelset has the potential to be equipped in urban rail transit. As a crucial part of the running gear, its dynamic characteristics directly affect the railway vehicle's stability and curve negotiation ability. This study follows a model–simulation–experiment method to delve into the dynamic process and steady convergent process of the independently rotating wheelset. An improved mathematical dynamic model of the independently rotating wheelset is established, considering the gravitational restoring forces of the wheelset and different creepages between the left and right wheels. In addition, the gyroscopic effects on the independently rotating wheelset with positive wheel tread conicity and at high speeds are introduced and analyzed. With variations in the longitudinal speed and yaw suspension coefficients, three kinds of motions, derailment, hunting, and offset running, occur on the independently rotating wheelset. We find that the gyroscopic effects contribute to the slight self-guidance ability of the independently rotating wheelset, causing a hunting motion at high speeds. Through sufficient simulations, the improved mathematical dynamic model is verified to be closer to the dynamic model built in the general multibody system simulation software SIMPACK 2018 than the classical mathematical dynamic model. Further, we perform experiments on a scaled independently rotating wheelset experiment system. The dynamic characteristics derived from theoretical analysis, especially the slight self-guidance ability at high speeds, are verified.

Keywords: independently rotating wheelset; independently rotating wheels; yaw suspension; gravitational restoring force; gyroscopic effects; self-guidance ability

Citation: Jia, X.; Yin, Y.; Wang, W. Dynamic Modeling, Dynamic Characteristics, and Slight Self-Guidance Ability at High Speeds of Independently Rotating Wheelset for Railway Vehicles. *Appl. Sci.* **2024**, *14*, 1548. https://doi.org/10.3390/app14041548

Academic Editors: Peter Gaspar and Junnian Wang

Received: 22 December 2023
Revised: 7 February 2024
Accepted: 8 February 2024
Published: 15 February 2024

1. Introduction

Light rail vehicles have been popularly applied in urban transportation systems due to their high capacity, safety, and reliability, which satisfy the needs of mass passenger transportation. To meet low-floor requirements and lightweight demands, independently rotating wheelset (IRW) technology is introduced in running mechanisms and widely studied. At the initial stage of IRW technology development, some advantages were thought to exist with the IRW, such as increased critical hunting speed, reduced rail and wheel flange wear, and improved curve negotiation performance [1,2]. However, with more and more research and attempts for IRW's applications, some fatal disadvantages have been discovered, including unique zigzag-type vibration, severe flange contact, and aggravated wear problems [3–5].

In contrast to the conventional solid wheelset (SW), the two wheels of an IRW can rotate at different angular speeds. Then, the compensation of the path difference between the inner and outer wheel unnecessarily depends on the lateral displacement and the wheel tread conicity, which theoretically improves the curve negotiation performance of the IRW. However, decoupling the two wheels in the rotational direction leads to a loss of longitudinal creep moment, causing self-guidance-ability deficiency on the IRW. Although many methods were investigated and developed to improve the self-guidance ability of the IRW [6–14], only a few studies have focused on the intrinsic dynamic characteristics and the fundamental reasons why the self-guidance ability deficiency happens on the IRW.

Goodall and Li [15] analyzed an unconstrained IRW model using the block diagram method and made a comparison with the SW model on stability issues. The theoretical frequency expression shows that on the IRW, the dynamic coupling via inertial effects can cause a kinematic oscillation. Sugiyama et al. [16] developed a multibody IRW model and conducted numerical simulations. The results demonstrated that in the change in wheel rolling radius, longitudinal slip can occur and contribute to a weak coupling of the lateral, yaw, and pitch motions. Y. Cho and J. Kwak [5] deduced mathematical IRW wheelset models and IRW bogie models with different settings of DOF and under consideration of gravitational restoring forces. According to simulation results on a tangent track, flange contact can be avoided under the restoration effects generated by gravitational restoring forces. To some extent, these theoretical and mathematical analyses of the IRW model are intrinsically and logically reasonable. However, due to some issues with hypothesis and research focus, they remain to be verified by specialized simulation software and experiments.

Most researchers and engineers considered that the hunting motion was eliminated on the IRW in previous research, but the hunting phenomenon on the IRW has already been observed in some simulations or practical experiments conducted by different research groups. Liang and Iwnicki [17] built an IRW simulation model in Simulink and an IRW experiment system with a test rig. They found that lateral oscillation would occur at high speeds without an active motor control. Ji et al. [18] developed an active steering control method for the IRW using hub motor wheels with rotating speed difference feedback. Their IRW model was built in the software SIMPACK. In their simulation results, when the output rotating speed fluctuation of the motor was 0.5%, the lateral displacement of the wheelset fluctuated back and forth around the center line of the rail, which is similar to the hunting motion on the SW. Yang et al. [19] designed a new type of bogie with four independently rotating wheels by taking advantage of the caster angle. They also found similar hunting motion on their experimental scaled IRW bogie.

As to an object rotating or spinning at high speeds, a special kind of stability around its rotation axis can be generated, such as spins and propellers, of which the phenomenon is generally called the gyroscopic effect in physics. Kurzeck et al. [20] used the gyroscopic effect mechanism to explain why the maximum torque values are required when getting through the transition curves. They found that the gyroscopic moment is related to an additional rotational velocity around the x-axis caused by the superelevation ramp of the track. However, whether the gyroscopic effects exist on the IRW with both two wheels rotating at high speeds on straight tracks or what unique dynamic characteristics would appear at high speeds were not deeply investigated before.

Motivated by the above considerations, the present study deduced an improved mathematical model of the IRW through the Euler–Lagrange dynamic analysis method. Considering that the translational forward speeds of the wheels are different, the creepages and creep forces were calculated separately on the wheels of each side. The effects of gravitational restoring forces and gyroscopic moment were also considered. Then, comparisons with a model generated in the software SIMPACK 2018 were conducted to verify the validity of the mathematical model. Further, the dynamic characteristics were analyzed and summarized with variations in the longitudinal speed and yaw suspension coefficients. In addition, a scaled IRW experiment system was built to observe and verify the existence of the dynamic characteristics, especially the slight self-guidance ability at high speeds.

2. Mathematical Dynamic Model of the IRW

As shown in Figure 1, a concept model of the IRW is introduced to deduce mathematical models and study its dynamic characteristics. For lateral dynamics analysis, an IRW can be simplified into three main parts: a left wheel, a right wheel, and a carrier of the two wheels. Under constraints of the bearings between the carrier and wheels, only relative rotation is allowed. Under constraints of contact patches between rail and wheels, the contact position of each wheel should obey the geometric profile in three dimensions. Additionally, under the constraint of the rail gauge, two sides of the wheel–rail contact patches have a positional relationship between each other. Then, the IRW's degrees of freedom (DOF) can be obtained as

$$\mathrm{DOF} = 6 \times 3 - 5 \times 2 - 1 \times 2 - 1 = 5 \tag{1}$$

Considering the situation of constant longitudinal velocity, four DOFs are taken into account to describe the lateral motion of an IRW on a straight rail track. We choose four generalized states, including the lateral displacement y, yaw angle ψ, rotational speed of the left wheel ω_{L}, and rotational speed of the right wheel ω_{R}. To substitute for the connection between the wheelset carrier and the two-axle bogie's frame and to study the IRW's dynamic characteristics separately, a 'virtual joint' is set moving with the IRW along the center of the rail track, shown in Figure 1b. The pitch angle of the wheelset is assumed to be constrained to zero with respect to this 'virtual joint'. In addition, a yaw suspension system with springs and dampers is also installed between the wheelset and this 'virtual joint'.

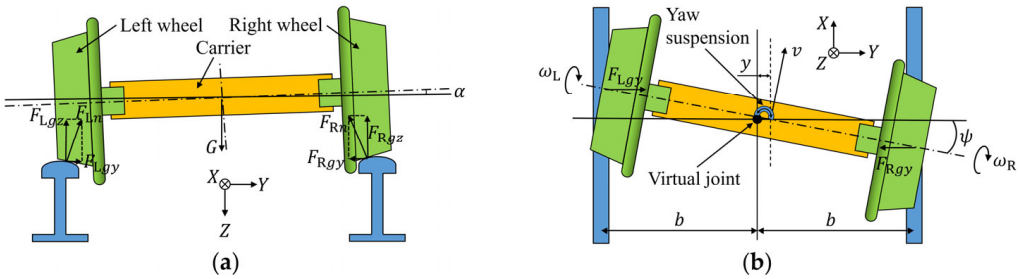

Figure 1. The IRW model. (**a**) Back view; (**b**) top view.

Generally, in the force analysis process of conventional wheelsets for lateral dynamics research, only creep, spring, damping, and inertia forces are considered. Under the considerable influence of longitudinal creep forces, the effects of gravitational restoring forces are often simplified or omitted. However, it is widely regarded that the effects of longitudinal creep forces on the IRW's lateral dynamics are negligible. Then, some forces simplified or omitted before may regain dominance in the IRW's motion. In this study, the influences of gravitational restoring forces and gyroscopic moment are considered. They are introduced in Sections 2.2 and 2.3, respectively.

2.1. Creep Force

For an IRW, the left wheel, right wheel, and carrier are three different parts of the mechanical system, which means that the translational forward speeds of these three parts are also different from each other, resulting in different creepages on the left wheel and the right wheel, so the creep forces applied on the left wheel and the right wheel should be calculated separately.

Considering the yaw speed $\dot{\psi}$ of the carrier, the longitudinal forward speeds of the left wheel and the right wheel can be derived as follows, v_{L} and v_{R}, respectively.

$$\begin{cases} v_{\mathrm{L}} = v + b\dot{\psi} \\ v_{\mathrm{R}} = v - b\dot{\psi} \end{cases} \tag{2}$$

where v is the longitudinal forward speed of the carrier, and b is half the lateral distance between the left and right wheels.

When calculating creep forces acting on the contact patches of the IRW model on the rail, these two different longitudinal forward speeds are adopted to improve model accuracy, which makes it different from the SW in the creep force calculation [21]. For example, to calculate the lateral creep force generated by the lateral speed for a SW, the force is given by

$$F_{cy(\dot{y})} = -2k_{22}\frac{\dot{y}}{v} \tag{3}$$

while on the IRW model, the left wheel, right wheel, and carrier are three different parts of the mechanical system, meaning three different translational speeds; thus, this creep force should be written as

$$F_{cy(\dot{y})} = F_{\mathrm{L}cy(\dot{y})} + F_{\mathrm{R}cy(\dot{y})} = -k_{22}\frac{\dot{y}}{v + b\dot{\psi}} - k_{22}\frac{\dot{y}}{v - b\dot{\psi}} \tag{4}$$

where k_{22} is the lateral Kalker's creep coefficient.

Other creep forces can be deduced as this pattern similarly. They are shown in Equations (28)–(31) at the end of Section 2.4 in detail.

2.2. Gravitational Restoring Force

Due to the conicity of wheel tread, the normal forces of both wheels are not strictly in the direction of gravity, so they have lateral components generally named gravitational restoring forces. As shown in Figure 1a,b and marked as $F_{\mathrm{L}gy}$ and $F_{\mathrm{R}gy}$, these two forces will work in the lateral and yaw movement, so they should be considered in the IRW model.

If a linear conicity wheel tread is adopted, the contact angle of the left wheel and the right wheel related to y can be defined as follows, $\delta_{\mathrm{L}}(y)$ and $\delta_{\mathrm{R}}(y)$, respectively

$$\begin{cases} \delta_{\mathrm{L}}(y) = \delta_0 - \frac{\lambda}{b}y = \lambda\left(1 - \frac{y}{b}\right) \\ \delta_{\mathrm{R}}(y) = \delta_0 + \frac{\lambda}{b}y = \lambda\left(1 + \frac{y}{b}\right) \end{cases} \tag{5}$$

where δ_0 is the nominal contact angle at the center position, and λ is the equivalent wheel–rail tread conicity at the center position.

It is assumed that besides the whole gravity force of the IRW itself, there exist extra vertical loads virtually from the bogie or the vehicle acting on the left and right wheels, $F_{\mathrm{L}z}$ and $F_{\mathrm{R}z}$, respectively. The resultant gravitational restoring force of the IRW can be expressed as follows

$$\begin{aligned} F_{gy} = F_{\mathrm{L}gy} - F_{\mathrm{R}gy} &= \frac{(m_{\mathrm{C}}+2m_{\mathrm{W}})g+F_{\mathrm{L}z}+F_{\mathrm{R}z}}{2}[\delta_{\mathrm{L}}(y) - \delta_{\mathrm{R}}(y)] \\ &= -((m_{\mathrm{C}} + 2m_{\mathrm{W}})g + F_{\mathrm{L}z} + F_{\mathrm{R}z})\frac{\lambda y}{b} \end{aligned} \tag{6}$$

where m_{C} is the carrier mass, m_{W} is the wheel mass, and g is the gravitational acceleration.

Additionally, the moment generated by the gravitational restoring forces can be expressed as follows

$$M_{g\psi} = F_{\mathrm{L}gy}b\psi + F_{\mathrm{R}gy}b\psi = ((m_{\mathrm{C}} + 2m_{\mathrm{W}})g + F_{\mathrm{L}z} + F_{\mathrm{R}z})\lambda b\psi \tag{7}$$

According to Equation (6), force F_{gy} and lateral displacement y present a negative relation, while according to Equation (7), moment $M_{g\psi}$ and yaw angle ψ present a positive relation. In view of this, force F_{gy} is generally regarded as a factor contributing to IRW's self-centering ability, and moment $M_{g\psi}$ is usually considered a cause for the IRW's derailment at low speeds, as shown in Figure 2. These two viewpoints will be verified later.

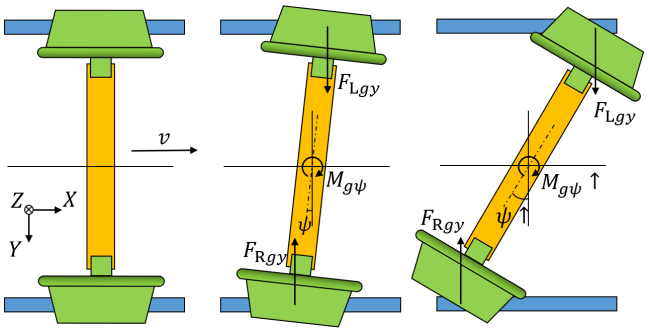

Figure 2. Derailment motion caused by gravitational restoring moment $M_{g\psi}$.

2.3. Gyroscopic Moment

Strictly analyzing the rotation of the wheels, it is a relative rotational motion in the carrier reference system. Due to the carrier's yaw and roll movements, although the IRW rides at a constant forward velocity on the rail, the carrier coordinate system is a non-inertial reference coordinate. In addition, the three angular motions of the IRW are orthometric to each other. Then, some coupling effects exist between the wheels and the IRW. When the wheels rotate at high speeds, we find that the IRW will regain slight self-guidance ability to resist the derailment tendency caused by the gravitational restoring moment. This phenomenon has the same pattern of mechanisms as the gyroscopic effects on a top spinning at high speeds, which makes the spin top resist the gravity effects and not fall down to the ground.

Figure 3 demonstrates a tiny rolling angle change $d\alpha$ of the IRW from position A to position B after a little time gap dt. Let $\vec{a}$, $\vec{b}$, and $\vec{c}$ denote the unit direction vectors of the wheel axle at position A, the wheel axle at position B, and the rolling axis of the IRW, respectively. The unit direction vector of the wheel axle at position B can be derived as

$$\vec{b} = \vec{a} + \dot{\alpha} dt \left(\vec{c} \times \vec{a} \right) \tag{8}$$

where $\dot{\alpha}$ is the instantaneous rolling angular speed.

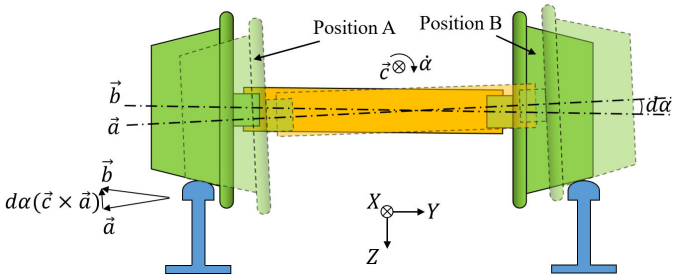

Figure 3. The IRW running on the rail track with its roll angle changing from position A to B.

Because both sides of the wheels rotate in the same direction when the IRW is riding forward, the angular momentum magnitude of the wheels is given by

$$H = H_{\mathrm{L}} + H_{\mathrm{R}} = J_{\mathrm{W}y}(\omega_{\mathrm{L}} + \omega_{\mathrm{R}}) \tag{9}$$

where $J_{\mathrm{W}y}$ is the inertia moment of wheel in the y axle.

The variation in this angular momentum can be deduced as

$$d\vec{H} = (H + dH)\vec{b} - H\vec{a} = H\dot{\alpha} dt \left(\vec{c} \times \vec{a} \right) + dH\vec{b} \tag{10}$$

Then, the derivation of $\vec{H}$ with respect to time t can be obtained as

$$\frac{d\vec{H}}{dt} = \left(\dot{\alpha}\vec{c}\right) \times \left(H\vec{a}\right) + \frac{dH}{dt}\vec{b} = \vec{\dot{\alpha}} \times \vec{H} + \frac{dH}{dt}\vec{b} \tag{11}$$

When the IRW rides at a constant longitudinal forward speed, the angular momentum magnitude H does not change, which means that

$$\frac{dH}{dt} = 0 \tag{12}$$

Then, the derivation of $\vec{H}$ with respect to time t can be written as

$$\frac{d\vec{H}}{dt} = \vec{\dot{\alpha}} \times \vec{H} \tag{13}$$

Equation (13) shows that the existence of the rolling angular speed results in the variation in the angular momentum of the two wheels. Furthermore, the direction of this cross product is coincidentally the same as the yaw angular direction of the IRW. According to mechanical principles, a gyroscopic moment exists to resist the direction change of $\vec{H}$ and to maintain its original rotational direction, which means that the gyroscopic moment is in the yaw angular direction of the IRW, and its magnitude is

$$M_{\mathrm{G}} = \left| -\frac{d\vec{H}}{dt} \right| = J_{\mathrm{W}y}\dot{\alpha}(\omega_{\mathrm{L}} + \omega_{\mathrm{R}}) \tag{14}$$

If both two wheels with positive linear conicity tread are installed on the carrier, the roll velocity $\dot{\alpha}$ will present a negative linear relationship with lateral displacement speed $\dot{y}$, which can be determined by the IRW's geometric parameters and given by

$$\dot{\alpha} = -\frac{\lambda}{b}\dot{y} \tag{15}$$

Then, M_{G} with adaptation of positive linear conicity tread wheels can be written as

$$M_{\mathrm{G}} = -\frac{\lambda J_{\mathrm{W}y}}{b}\dot{y}(\omega_{\mathrm{L}} + \omega_{\mathrm{R}}) \tag{16}$$

Moment M_{G} is the gyroscopic moment in the yaw direction of the IRW, and its magnitude is relative to the carrier's lateral translational speed and the wheels' rotational angular speeds.

The effects brought out by gyroscopic moment can be analyzed through Equation (16) and can also be described visually in Figure 4. When the positive linear tread conicity wheels are adopted, lateral velocity $\dot{y}$ and gyroscopic moment M_{G} present an opposite reaction, which forms a type of self-guidance ability on the IRW, and the derailment tendency can be resisted. According to Equation (16), a large equivalent wheel tread conicity and high wheel rotational speeds are necessary for acquiring a dominant self-guidance ability. Furthermore, compared to the inertia moment of the whole IRW in the yaw direction, the inertia moment of the wheel in the y direction is much smaller. Thus, the self-guidance ability caused by gyroscopic effects is relatively slight to some extent, especially at low longitudinal speeds. However, due to the loss of longitudinal creep moment on the IRW, the gyroscopic moment can significantly affect the dynamic characteristics of the IRW, especially at high longitudinal speeds. The existence verification of the self-guidance ability caused by gyroscopic effects through simulations, as well as experiments, and how the gyroscopic moment affects the lateral dynamics of the IRW will be demonstrated in Sections 3–5.

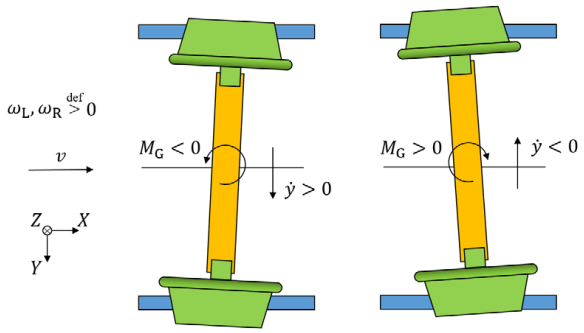

Figure 4. Slight self-guidance ability under gyroscopic effects.

2.4. IRW Model Deduction

We only consider the IRW rides on a straight, flat rail track at constant longitudinal speeds, so the coordinate system accompanying the IRW along the rail track center is an inertial reference system. Then, the dynamic equations can be set up in this coordinate system through the Euler–Lagrange approach.

The kinetic energy of the carrier for lateral dynamics analysis is

$$T_C = \frac{1}{2}m_C\dot{y}^2 + \frac{1}{2}J_{Cx}\dot{\alpha}^2 + \frac{1}{2}J_{Cz}\dot{\psi}^2 = \frac{1}{2}\left(\frac{\lambda^2}{b^2}J_{Cx} + m_C\right)\dot{y}^2 + \frac{1}{2}J_{Cz}\dot{\psi}^2 \tag{17}$$

where J_{Cx} and J_{Cz} are carrier's inertia moments in the x and z directions, respectively.

The angular kinetic energy of the left wheel in its rotation direction around its axle is

$$T_{L\theta} = \frac{1}{2}J_{Wy}\omega_L^2 \tag{18}$$

Additionally, the wheel also moves with the carrier in translational and angular directions. The translational kinetic energy of the left wheel in the IRW's lateral direction is

$$T_{Ly} = \frac{1}{2}m_W\dot{y}^2 \tag{19}$$

According to the Koenig theorem, the angular kinetic energy of the left wheel in the IRW's yaw direction is

$$T_{L\psi} = \frac{1}{2}J_{Wz}\dot{\psi}^2 + \frac{1}{2}m_W\left(b\dot{\psi}\right)^2 = \frac{1}{2}\left(J_{Wz} + m_W b^2\right)\dot{\psi}^2 \tag{20}$$

where J_{Wz} is the wheel's inertia moment in the z direction.

Similarly, the angular kinetic energy of the left wheel in the IRW's roll direction is

$$T_{L\alpha} = \frac{1}{2}\left(J_{Wx} + m_W b^2\right)\dot{\alpha}^2 \tag{21}$$

where J_{Wx} is the wheel's inertia moment in the x direction.

Then, the total kinetic energy of the left wheel is

$$\begin{aligned} T_L &= T_{Ly} + T_{L\psi} + T_{L\alpha} + T_{L\theta} \\ &= \tfrac{1}{2}\left((1+\lambda^2)m_W + \tfrac{\lambda^2}{b^2}J_{Wx}\right)\dot{y}^2 + \tfrac{1}{2}\left(J_{Wz} + m_W b^2\right)\dot{\psi}^2 + \tfrac{1}{2}J_{Wy}\omega_L^2 \end{aligned} \tag{22}$$

Similarly, the total kinetic energy of the right wheel is

$$T_R = \frac{1}{2}\left(\left(1+\lambda^2\right)m_W + \frac{\lambda^2}{b^2}J_{Wx}\right)\dot{y}^2 + \frac{1}{2}\left(J_{Wz} + m_W b^2\right)\dot{\psi}^2 + \frac{1}{2}J_{Wy}\omega_R^2 \tag{23}$$

The total kinetic energy of the IRW is

$$\begin{aligned} T = T_{\mathrm{C}} + T_{\mathrm{L}} + T_{\mathrm{R}} = \tfrac{1}{2}\Big(m_{\mathrm{C}} + 2\big(1+\lambda^2\big)m_{\mathrm{W}} + \tfrac{\lambda^2}{b^2}J_{\mathrm{C}x} + \tfrac{2\lambda^2}{b^2}J_{\mathrm{W}x}\Big)\dot{y}^2 \\ + \tfrac{1}{2}\big(J_{\mathrm{C}z} + 2J_{\mathrm{W}z} + 2m_{\mathrm{W}}b^2\big)\dot{\psi}^2 + \tfrac{1}{2}J_{\mathrm{W}y}\omega_{\mathrm{L}}^2 + \tfrac{1}{2}J_{\mathrm{W}y}\omega_{\mathrm{R}}^2 \end{aligned} \tag{24}$$

Assuming the linear conical wheel rides on a knife-edged rail and a yaw angular spring with stiffness coefficient K_ψ is installed, the total potential energy of the IRW is

$$V = V_{\mathrm{C}g} + V_{\mathrm{L}g} + V_{\mathrm{R}g} + V_\psi = 0 + m_{\mathrm{W}}g(-\lambda y) + m_{\mathrm{W}}g\lambda y + \frac{1}{2}K_\psi\psi^2 = \frac{1}{2}K_\psi\psi^2 \tag{25}$$

Assuming a yaw damper with damping coefficient C_ψ is installed, the dissipation energy of the IRW is

$$D = \frac{1}{2}C_\psi\dot{\psi}^2 \tag{26}$$

According to Euler–Lagrange mechanics theorem, the dynamic equations for a mechanical system can be expressed as follows

$$\frac{d}{dt}\frac{\partial T}{\partial \dot{q}_i} - \frac{\partial T}{\partial q_i} + \frac{\partial V}{\partial q_i} + \frac{\partial D}{\partial \dot{q}_i} = Q_i \tag{27}$$

where t represents time, q_i represents generalized coordinates, $\dot{q}_i$ represents generalized velocities, and Q_i represents generalized forces.

Then, the dynamic equations of the IRW for lateral dynamics analysis can be expressed in detail as follows

$$\begin{aligned} \Big(m_{\mathrm{C}} + 2\big(1+\lambda^2\big)m_{\mathrm{W}} + \tfrac{\lambda^2}{b^2}J_{\mathrm{C}x} + \tfrac{2\lambda^2}{b^2}J_{\mathrm{W}x}\Big)\ddot{y} + k_{22}\tfrac{\dot{y}}{v+b\dot{\psi}} + k_{22}\tfrac{\dot{y}}{v-b\dot{\psi}} \\ + \big((m_{\mathrm{C}} + 2m_{\mathrm{W}})g + F_{\mathrm{L}z} + F_{\mathrm{R}z}\big)\tfrac{\lambda}{b}y - 2k_{22}\psi = 0 \end{aligned} \tag{28}$$

$$\begin{aligned} \big(J_{\mathrm{C}z} + 2J_{\mathrm{W}z} + 2m_{\mathrm{W}}b^2\big)\ddot{\psi} + C_\psi\dot{\psi} + K_\psi\psi - \big((m_{\mathrm{C}} + 2m_{\mathrm{W}})g + F_{\mathrm{L}z} + F_{\mathrm{R}z}\big)\lambda b\psi \\ + \tfrac{\lambda J_{\mathrm{W}y}}{b}\dot{y}(\omega_{\mathrm{L}} + \omega_{\mathrm{R}}) - k_{11}b\left(\tfrac{\omega_{\mathrm{L}}(r_0-\lambda y) - \left(v+b\dot{\psi}\right)}{v+b\dot{\psi}} - \tfrac{\omega_{\mathrm{R}}(r_0+\lambda y) - \left(v-b\dot{\psi}\right)}{v-b\dot{\psi}}\right) = 0 \end{aligned} \tag{29}$$

$$J_{\mathrm{W}y}\dot{\omega}_{\mathrm{L}} + k_{11}r_0\frac{\omega_{\mathrm{L}}(r_0-\lambda y) - \left(v+b\dot{\psi}\right)}{v+b\dot{\psi}} = 0 \tag{30}$$

$$J_{\mathrm{W}y}\dot{\omega}_{\mathrm{R}} + k_{11}r_0\frac{\omega_{\mathrm{R}}(r_0+\lambda y) - \left(v-b\dot{\psi}\right)}{v-b\dot{\psi}} = 0 \tag{31}$$

where k_{11} is the longitudinal Kalker's creep coefficient.

Due to the consideration of both the gravitational restoring forces and gyroscopic effects, we name this mathematical model the G2-IRW model.

2.5. Steady States Analysis

If the IRW system described by Equations (28)–(31) can be stabilized by the yaw spring and yaw damper, the steady-state solution of the dynamics equations will represent the steady characteristics of the IRW.

When steady, the translational and angular accelerations of the IRW are zero, that is, $\ddot{y} = 0$, $\ddot{\psi} = 0$, $\dot{\omega}_{\mathrm{L}} = 0$, and $\dot{\omega}_{\mathrm{R}} = 0$. Whether $\dot{y}$ is zero or not and whether $\dot{\psi}$ is zero or not is unknown at the beginning of the analysis. Assuming that $\dot{\psi} \neq 0$, which means that $\dot{\psi} = \text{const}$, noted as $\dot{\psi} = \dot{\psi}_0$, then if the IRW reaches steady states after time t_s, the yaw angle ψ varying with time t can be expressed as follows

$$\psi(t) = \dot{\psi}_0 \cdot (t - t_s) + \psi(t_s) \tag{32}$$

Substituting Equation (32) into Equation (28), we can find that the lateral speed $\dot{y}$ varies with time t, which contradicts with $\ddot{y} = 0$. Then, $\dot{\psi} = 0$ can be deduced.

According to Equation (30), when $\dot{\omega}_{\mathrm{L}} = 0$, we can deduce that

$$\omega_{\mathrm{L}}(r_0 - \lambda y) - \left(v + b\dot{\psi}\right) = 0 \tag{33}$$

which can be rearranged as

$$\omega_{\mathrm{L}} = \frac{v + b\dot{\psi}}{r_0 - \lambda y} = \frac{v}{r_0 - \lambda y} \tag{34}$$

Similarly, we can also obtain

$$\omega_{\mathrm{R}} = \frac{v - b\dot{\psi}}{r_0 + \lambda y} = \frac{v}{r_0 + \lambda y} \tag{35}$$

The Taylor expansion of Equations (34) and (35) at $y = 0$ are expressed as follows, respectively

$$\begin{cases} \omega_{\mathrm{L}} = \frac{v}{r_0 - \lambda y} = \frac{v}{r_0}\left(1 + \frac{\lambda y}{r_0} + \left(\frac{\lambda y}{r_0}\right)^2 + \left(\frac{\lambda y}{r_0}\right)^3 + \cdots\right) \\ \omega_{\mathrm{R}} = \frac{v}{r_0 + \lambda y} = \frac{v}{r_0}\left(1 - \frac{\lambda y}{r_0} + \left(\frac{\lambda y}{r_0}\right)^2 - \left(\frac{\lambda y}{r_0}\right)^3 + \cdots\right) \end{cases} \tag{36}$$

Generally, $\lambda y < 0.1 r_0$, so the higher-order items can be omitted, and then the differential rotational speed of the two wheels $\Delta\omega$ can be deduced as

$$\Delta\omega = \omega_{\mathrm{L}} - \omega_{\mathrm{R}} = \frac{2\lambda v}{r_0^2} y \tag{37}$$

Based on the analysis above, Equation (29) can be simplified as

$$K_\psi \psi - ((m_{\mathrm{C}} + 2m_{\mathrm{W}})g + F_{\mathrm{L}z} + F_{\mathrm{R}z})\lambda b\psi + \frac{\lambda J_{\mathrm{W}y}}{b}\dot{y}(\omega_{\mathrm{L}} + \omega_{\mathrm{R}}) = 0 \tag{38}$$

Consider the situation where $K_\psi \gg ((m_{\mathrm{C}} + 2m_{\mathrm{W}})g + F_{\mathrm{L}z} + F_{\mathrm{R}z})\lambda b$, then the yaw angle ψ can be obtained as

$$\psi = -\frac{\lambda J_{\mathrm{W}y}(\omega_{\mathrm{L}} + \omega_{\mathrm{R}})}{b\left(K_\psi - ((m_{\mathrm{C}} + 2m_{\mathrm{W}})g + F_{\mathrm{L}z} + F_{\mathrm{R}z})\lambda b\right)}\dot{y} \tag{39}$$

When steady, the lateral speed $\dot{y}$ should be quite low. Additionally, because the magnitude of the yaw stiffness is usually large enough, the coefficient in front of $\dot{y}$ is generally less than 0.1. Then, yaw angle ψ can be treated as zero when the IRW reaches steady states, that is

$$\psi = 0 \tag{40}$$

Then, Equation (28) can be simplified as

$$k_{22}\frac{\dot{y}}{v} + k_{22}\frac{\dot{y}}{v} + ((m_{\mathrm{C}} + 2m_{\mathrm{W}})g + F_{\mathrm{L}z} + F_{\mathrm{R}z})\frac{\lambda}{b}y = 0 \tag{41}$$

The relation between the lateral speed $\dot{y}$ and the lateral displacement y can be deduced as

$$\dot{y} = -\frac{\lambda v((m_{\mathrm{C}} + 2m_{\mathrm{W}})g + F_{\mathrm{L}z} + F_{\mathrm{R}z})}{2bk_{22}}y \tag{42}$$

Equation (42) is an ordinary differential equation, and if the IRW's dynamic oscillation is suppressed after time t_s, its solution can be expressed as

$$y(t) = y(t_s)\exp\left(-\frac{\lambda v((m_{\mathrm{C}} + 2m_{\mathrm{W}})g + F_{\mathrm{L}z} + F_{\mathrm{R}z})}{2bk_{22}}(t - t_s)\right) \tag{43}$$

In Equation (43), the coefficient in front of time duration $t - t_s$ is negative, which means that the lateral displacement $y(t_s)$ will decay and finally converge. Define this decay coefficient as η, that is

$$\eta = -\frac{\lambda v((m_C + 2m_W)g + F_{Lz} + F_{Rz})}{2bk_{22}} \tag{44}$$

The steady-states conclusions gather as follows

$$\ddot{y} = 0, \ddot{\psi} = 0, \dot{\omega}_L = 0, \dot{\omega}_R = 0, \dot{\psi} = 0, \psi = 0 \tag{45}$$

$$y(t) = y(t_s)\exp\left(-\frac{\lambda v((m_C + 2m_W)g + F_{Lz} + F_{Rz})}{2bk_{22}}(t - t_s)\right) \tag{46}$$

$$\Delta\omega = \omega_L - \omega_R = \frac{2\lambda v}{r_0^2}y \tag{47}$$

Equation (46) demonstrates that the lateral displacement y will exponentially converge to zero under the gravitational effects after time t_s, which means that the convergence rate decreases with the convergence of y. Thus, when y is quite close to zero, the convergence rate will be quite low as well. Additionally, the denominator of the decay coefficient η contains the lateral Kalker's creep coefficient k_{22}, of which the magnitude is large, resulting in a small decay coefficient. Additionally, a small wheel tread conicity λ is sometimes adopted. Therefore, although the lateral displacement y can converge to zero eventually, the convergence rate is very small, which makes y almost steady in a short duration of time. That is why the running trailer of the IRW is always offset to the center of the railway track, and only if the time duration is long enough, will the lateral displacement y converge to zero under the gravitational effects eventually.

Equation (47) shows a kinematic relation between differential rotational speed $\Delta\omega$ and lateral displacement y. The coefficient is relevant to the equivalent wheel–rail tread conicity λ, the velocity of the IRW v, and the nominal wheel radius r_0. This kinematic relation demonstrates the intrinsic law for the offset running phenomenon on the IRW. Due to the freedom of the two wheels in the rotation direction around their axles, the differential rotational speed of the IRW does not have to be zero because the lateral displacement y can compensate for it. When the steady state of the IRW changes, for example, the differential rotational speed $\Delta\omega$ changes from $\Delta\omega_1$ to $\Delta\omega_2$, and the lateral displacement y also changes from y_1 to y_2 along the kinematic relation described by Equation (47). Then, the IRW will adjust to a new balanced steady state $(y_2, \Delta\omega_2)$. Therefore, the freedom of the differential rotational speed on the IRW leads to the freedom of the lateral displacement. That is why the IRW can be balanced at any state pair $(y, \Delta\omega)$ as long as their kinematic relation can satisfy Equation (47). This phenomenon will be demonstrated later in the simulations and experiments.

Figure 5 shows three types of steady convergent motions. If the IRW runs along the center of the railway track, the motion is named centered running. If the IRW does not run along the center of the railway track and is with lateral displacement y, according to the analysis before, it will take a long time for the IRW to converge to the center of the railway track. The motion in this long-time duration is named offset running in this paper.

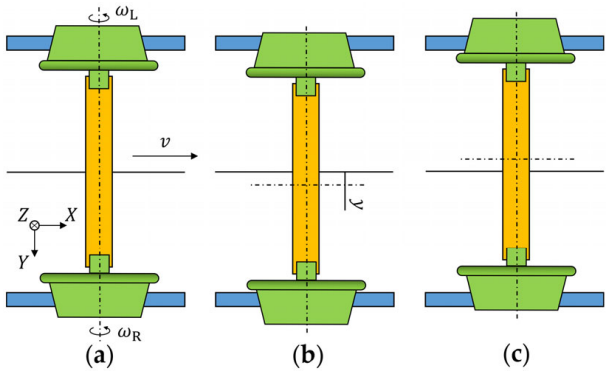

Figure 5. Three types of steady convergent motions. (**a**) Centered running ($y = 0$, $\omega_L = \omega_R$); (**b**) right-of-center offset running ($y > 0$, $\omega_L > \omega_R$); (**c**) left-of-center offset running ($y < 0$, $\omega_L < \omega_R$).

In this section, the creep forces of the two wheels are separately calculated for higher accuracy, the gravitational restoring forces are considered, and the gyroscopic effect can be theoretically proved through mechanics analysis. However, whether these three factors can significantly affect the IRW's dynamic characteristics still needs to be verified. In the next section, a classical IRW model is introduced without consideration of the three factors, and an IRW model built in the general multibody system simulation software SIMPACK 2018 is regarded as a criterion. The G2-IRW model deduced in Section 2.4 will be compared with them in detail.

3. Comparison of the Models

A type of classical IRW model has been presented in some research papers, which has been adopted to analyze the IRW dynamic characteristics and to design control methods. Concerning yaw suspension, the mostly adopted IRW model in these studies [2,16,17] can be expressed as follows

$$\begin{cases} m\ddot{y} + \frac{2k_{22}}{v}\dot{y} - 2k_{22}\psi = 0 \\ I\ddot{\psi} + \left(\frac{2b^2k_{11}}{v} + C_\psi\right)\dot{\psi} + K_\psi\psi - \frac{2br_0k_{11}}{v}\dot{\theta} + \frac{2b\lambda k_{11}}{r_0}y = 0 \\ I_W\ddot{\theta} + \frac{r_0^2k_{11}}{v}\dot{\theta} - \frac{br_0k_{11}}{v}\dot{\psi} - \lambda k_{11}y = 0 \end{cases} \tag{48}$$

where m is the total mass of the IRW, meaning $m = m_C + 2m_W$. $\dot{\theta}$ is defined as half differential rotational speed between the left and right wheels, meaning $2\dot{\theta} = \omega_L - \omega_R$. I is the total inertia moment of the IRW in the yaw direction, meaning $I = J_{Cz} + 2J_{Wz} + 2m_Wb^2$. I_W is the inertia moment of the wheel about its rotational axle, meaning $I_W = J_{Wy}$.

An IRW model built in the general multibody system simulation software SIMPACK 2018, as shown in Figure 6, is more approximate to the IRW in the real world and regarded as a criterion. The wheels adopt a 1/10 linear conicity tread with a 15 cm linear section in width, and the rails adopted the UIC60 shape. The wheel–rail contact analysis is demonstrated in Figure 7. A two-point contact between the rail and the wheel happens when y reaches about -32 mm.

In this section, the comparison results among the classical IRW model, the improved G2-IRW model deduced in Section 2.4, and the SIMPACK IRW model will be demonstrated and discussed. All these three simulation models were built with one set of physical parameters, shown in Table 1.

A number of running conditions were designed to validate the G2-IRW model and analyze the gravitational and gyroscopic effects. We considered the variations in the longitudinal speed, yaw stiffness, and yaw damping, which are listed in Tables 2–4, respectively. We chose nine representative conditions to demonstrate the results, including V1-S1-C1, V1-S6-C6, V1-S10-C10, V5-S1-C1, V5-S6-C6, V5-S10-C10, V10-S1-C1, V10-S6-C6, and V10-S10-C10. A 5 mm lateral displacement was given as the system's initial state step input, and then the IRW responses without any extra force and moment input.

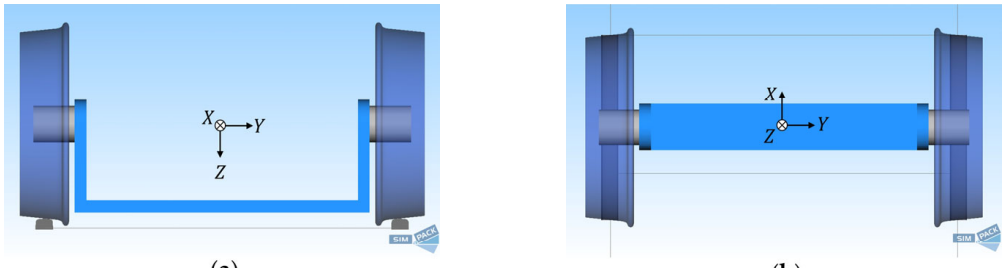

(**a**) (**b**)

Figure 6. The IRW model built in the software SIMPACK 2018. (**a**) Back view; (**b**) top view.

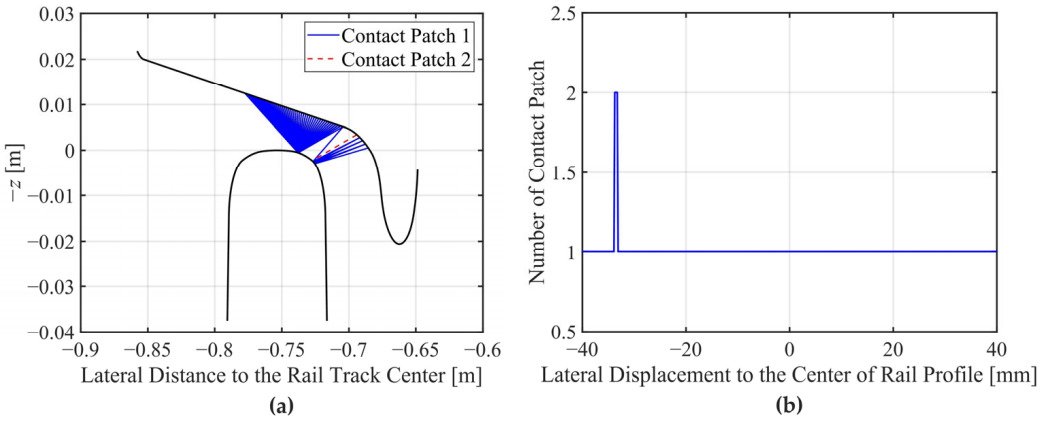

Figure 7. Wheel–rail contact analysis. (**a**) Contact patches with connection lines; (**b**) number of contact patches.

Table 1. The IRW's parameters in simulations.

Symbol	Definition	Value
m_C	Carrier mass	200 kg
m_W	Wheel mass	75 kg
J_{Cx}	Carrier's inertia moment in the x direction	35 kg·m^2
J_{Cy}	Carrier's inertia moment in the y direction	20 kg·m^2
J_{Cz}	Carrier's inertia moment in the z direction	30 kg·m^2
J_{Wx}	Wheel's inertia moment in the x direction	5 kg·m^2
J_{Wy}	Wheel's inertia moment in the y direction	8 kg·m^2
J_{Wz}	Wheel's inertia moment in the z direction	5 kg·m^2
b	Half lateral distance between the left and right wheels	0.72 m
r_0	Nominal wheel radius	0.4 m
λ	Equivalent wheel–rail tread conicity at the center position	0.1
k_{11}	Longitudinal Kalker's creep coefficient	4×10^6 N
k_{22}	Lateral Kalker's creep coefficient	6×10^6 N
g	Gravitational acceleration	9.81 m/s^2
F_{Lz}	Extra vertical loads on the left wheel	50 kN
F_{Rz}	Extra vertical loads on the right wheel	50 kN

Table 2. Simulation conditions of longitudinal speed.

No.	V1	V2	V3	V4	V5	V6	V7	V8	V9	V10
Velocity (m/s)	1	5	10	15	20	25	30	35	40	45

Table 3. Simulation conditions of yaw stiffness.

No.	S1	S2	S3	S4	S5	S6	S7	S8	S9	S10
Yaw Stiffness (kNm/rad)	0	2	5	10	20	50	100	200	500	1000

Table 4. Simulation conditions of yaw damping.

No.	C1	C2	C3	C4	C5	C6	C7	C8	C9	C10
Yaw Damping (kNms/rad)	0	0.02	0.05	0.1	0.2	0.5	1	2	5	10

As shown in Figure 8, at a low speed and without a yaw suspension, derailment happens on the IRW quickly and sharply. As analyzed in Section 2.2, the relation between

the yaw angle and the moment formed by gravitational restoring forces is positive feedback. Thus, a slight disturbance of the yaw angle can lead to a surging lateral deviation and divergent derailment.

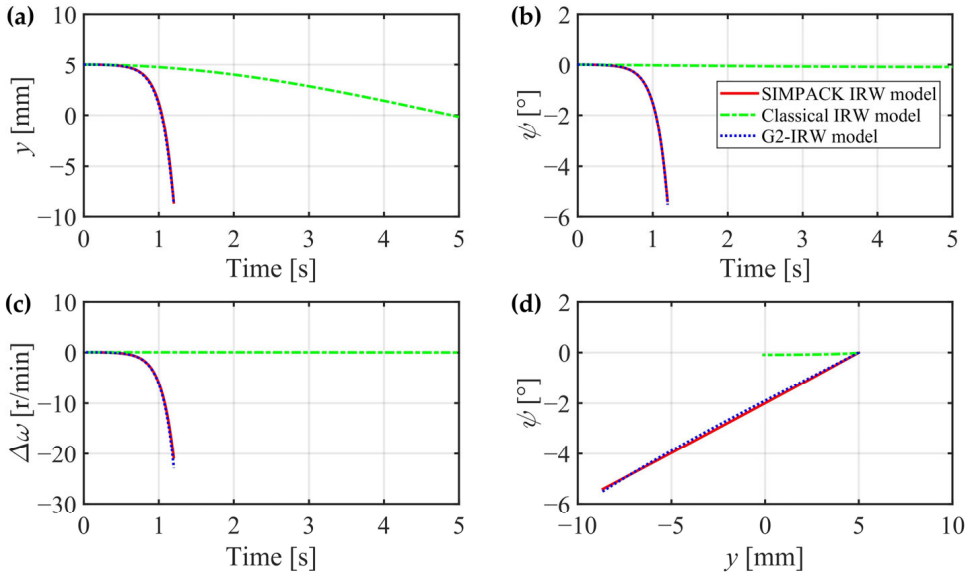

Figure 8. Lateral dynamics simulation results (V1-S1-C1). (**a**) Lateral displacement; (**b**) yaw angle; (**c**) differential wheel rotational speed; (**d**) $y - \psi$ phase diagram.

Figure 9 shows that at low speed and with a certain yaw suspension, the IRW slightly vibrates and finally converges. The vibrations of y and $\Delta\omega$ gradually disappear with a tendency toward zero, but the speed of the lateral convergence toward 0 is quite slow. By contrast, ψ converges to zero much more quickly. As analyzed in Section 2.5 and shown in Equations (45)–(47), ψ is 0, while y slowly converges to 0 during the steady convergent process.

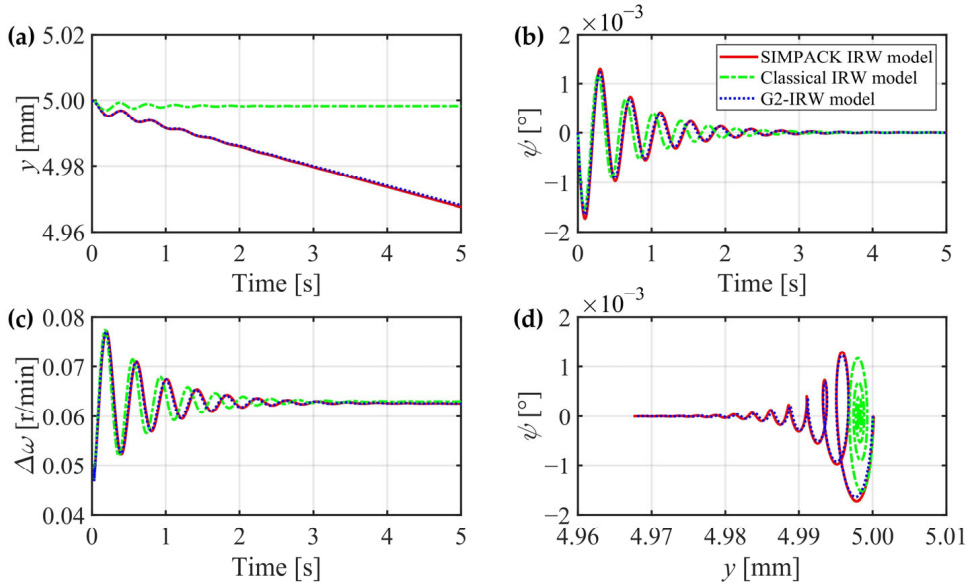

Figure 9. Lateral dynamics simulation results (V1-S6-C6). (**a**) Lateral displacement; (**b**) yaw angle; (**c**) differential wheel rotational speed; (**d**) $y - \psi$ phase diagram.

Figure 10 shows the simulation results with large yaw suspension parameters, leading to a sharp vibration at the beginning and immediately entering the steady convergent process. Compared with condition V1-S6-C6, adopting large yaw suspension parameters does not result in an intuitively quicker lateral convergence but almost the same lateral

convergence speed. That is because, in Equation (46), the steady convergent motion does not relate to the yaw suspension parameters. However, the large yaw suspension parameters affect the dynamic process at the beginning and shorten the vibration process before entering the steady convergent process.

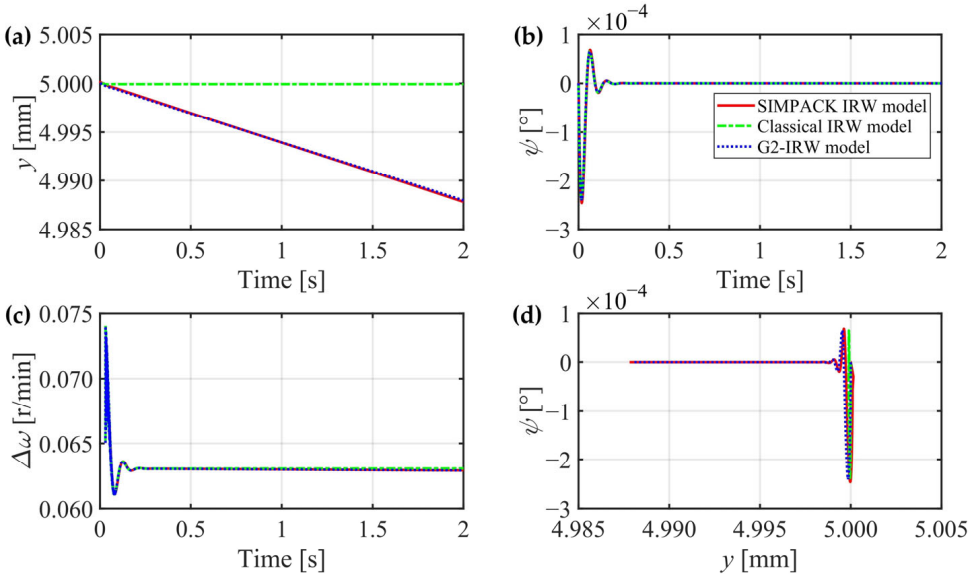

Figure 10. Lateral dynamics simulation results (V1-S10-C10). (**a**) Lateral displacement; (**b**) yaw angle; (**c**) differential wheel rotational speed; (**d**) $y - \psi$ phase diagram.

When the longitudinal speed increases to 20 m/s, the gyroscopic moment also increases and begins to gain the tendency to resist the derailment caused by the gravitational restoring moment. As shown in Figure 11, the yaw angle does not surge in one direction but bounces back after reaching the curve valley. The lateral displacement also tends to bounce back. However, due to the lateral displacement having already reached −32 mm, according to Figure 7, two-point contact between the rail and the left wheel will happen. Then, the dynamic process fundamentally changes and leads to another IRW's dynamic characters, which is out of remit in this paper.

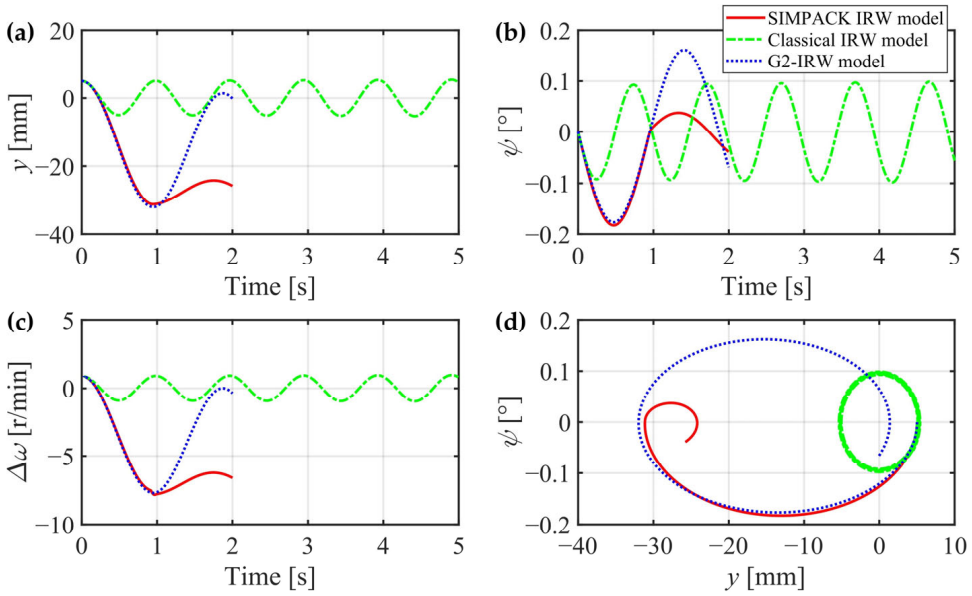

Figure 11. Lateral dynamics simulation results (V5-S1-C1). (**a**) Lateral displacement; (**b**) yaw angle; (**c**) differential wheel rotational speed; (**d**) $y - \psi$ phase diagram.

When yaw suspensions are added, as shown in Figure 12, the IRW enters the steady convergent process after some vibrations. The $y - \psi$ phase curve is a convergent spiral line with the yaw angle's damping at the beginning. When the vibration disappears, the $y - \psi$ phase curve turns into a straight line along axis $\psi = 0$ and toward the origin point $(y = 0, \psi = 0)$.

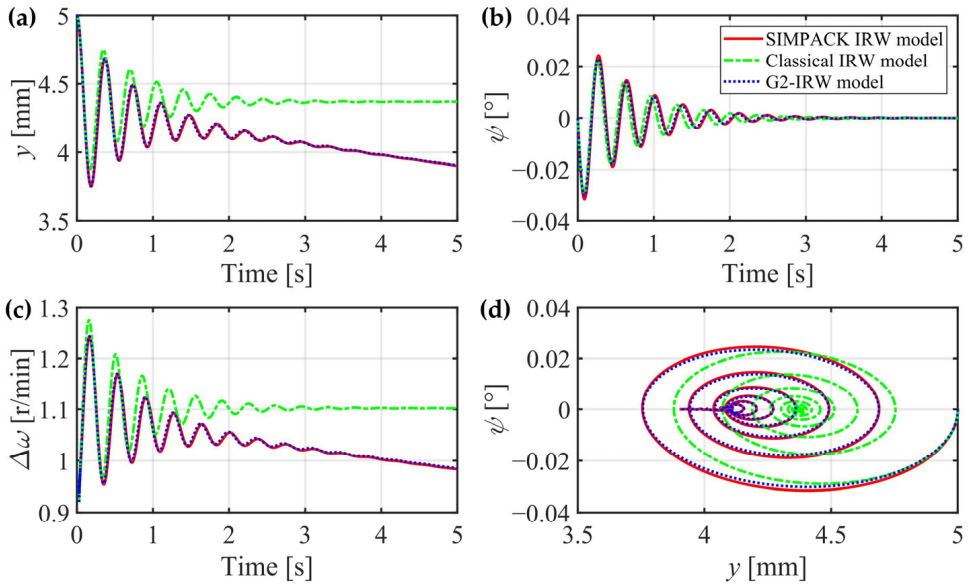

Figure 12. Lateral dynamics simulation results (V5-S6-C6). (**a**) Lateral displacement; (**b**) yaw angle; (**c**) differential wheel rotational speed; (**d**) $y - \psi$ phase diagram.

Figure 13 shows almost the same curve pattern as the condition V1-S10-C10. But at a faster longitudinal speed, the speed of the lateral convergence toward 0 is also faster than that at $v = 1$ m/s, which is in accordance with the analysis of Equation (46) in Section 2.5.

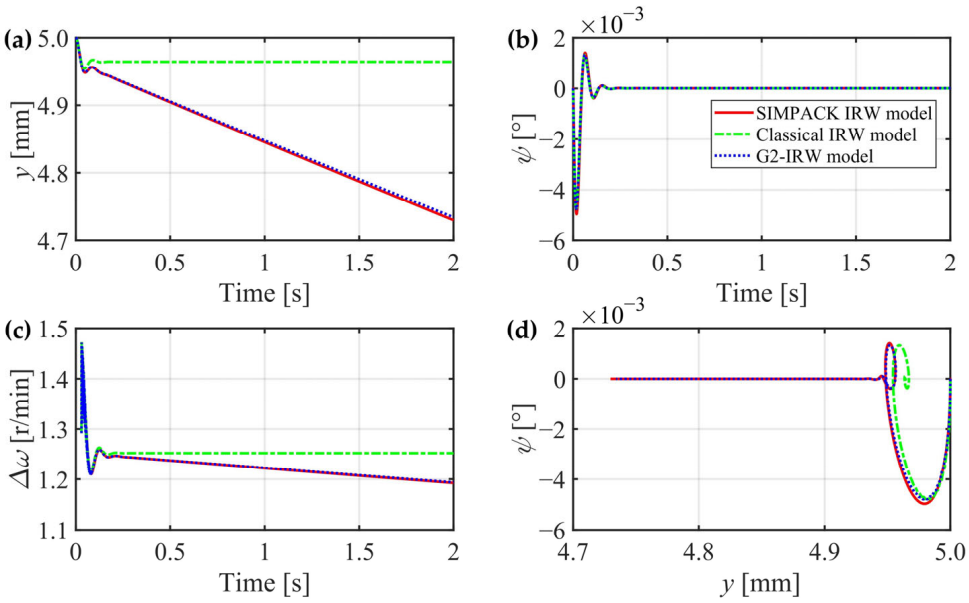

Figure 13. Lateral dynamics simulation results (V5-S10-C10). (**a**) Lateral displacement; (**b**) yaw angle; (**c**) differential wheel rotational speed; (**d**) $y - \psi$ phase diagram.

Figure 14 shows an interesting phenomenon on the IRW. When the longitudinal speed is fast enough, the IRW regains self-guidance ability on the straight track without yaw suspension. As analyzed in Section 2.3, owing to gyroscopic effects, if the angular

momentum of the wheels is large enough, the direction of the angular momentum regains self-stabilizing ability. For an IRW at high longitudinal speed, the derailment tendency caused by the gravitational restoring moment can be conquered by the gyroscopic moment. Then, the IRW regains self-guidance ability. This phenomenon is named the slight self-guidance ability of the IRW in this paper.

Although the IRW regains self-guidance ability at high longitudinal speeds, the gyroscopic effects can be suppressed by yaw suspension. As shown in Figure 15, the IRW enters the steady convergent process in 4 s with an initial step input of 5 mm lateral deviation. Under this condition, the yaw stiffness is 50 kNm/rad, and the yaw damping is 500 Nms/rad, which is just about 1% of the coefficients on a conventional bogie with SWs. In view of these results, for the IRW at high speeds, firstly, the self-guidance ability is regained owning to the gyroscopic effects. Secondly, the oscillation motion can be stabilized by yaw suspension with much smaller suspension coefficients, which makes the IRW much more accessible to pass curves with small radii than the SWs.

As demonstrated in Figure 16, the oscillation is almost completely suppressed with larger yaw suspension coefficients. In addition, at longitudinal speed $v = 45$ m/s, the speed of the lateral convergence toward 0 is much faster than that at $v = 1$ m/s.

If the simulation duration is expanded to 100 s, the whole steady convergent process can be demonstrated in Figure 17. The curves show the negative-exponential convergent process, as Equation (46) describes. Because the convergence duration is more than 60 s with initial step-input $y = 5$ mm and even at speed $v = 45$ m/s, an extra self-guidance control is necessary to be developed to speed up this convergent process. Especially if the longitudinal speed is too slow, such as during the standing start process, the convergence duration for the IRW may become too long to be practically acceptable. Thus, self-guidance control is crucially essential for the IRW at low speeds.

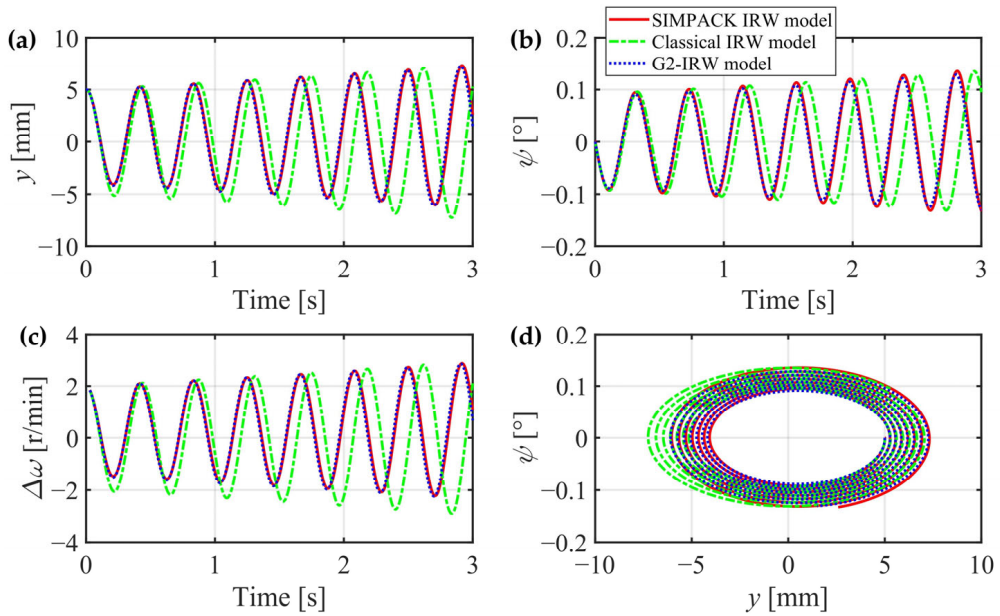

Figure 14. Lateral dynamics simulation results (V10-S1-C1). (**a**) Lateral displacement; (**b**) yaw angle; (**c**) differential wheel rotational speed; (**d**) $y - \psi$ phase diagram.

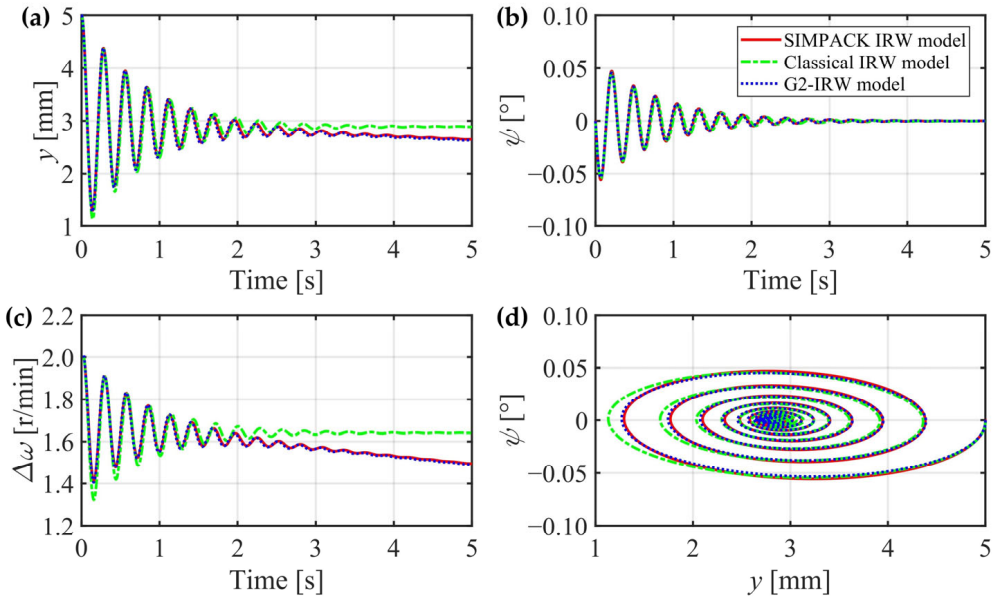

Figure 15. Lateral dynamics simulation results (V10-S6-C6). (**a**) Lateral displacement; (**b**) yaw angle; (**c**) differential wheel rotational speed; (**d**) $y - \psi$ phase diagram.

Under the above conditions, the simulation results of the G2-IRW model are verified close to the SIMPACK model, demonstrating that the G2-IRW model is more accurate than the classical IRW model. The significant effects of the gravitational restoring forces and gyroscopic moment analyzed in Sections 2.2 and 2.3, respectively, are verified by simulation results. The steady-states analysis in Section 2.5 and the detailed steady convergent process described by Equations (45)–(47) are also verified by simulation results.

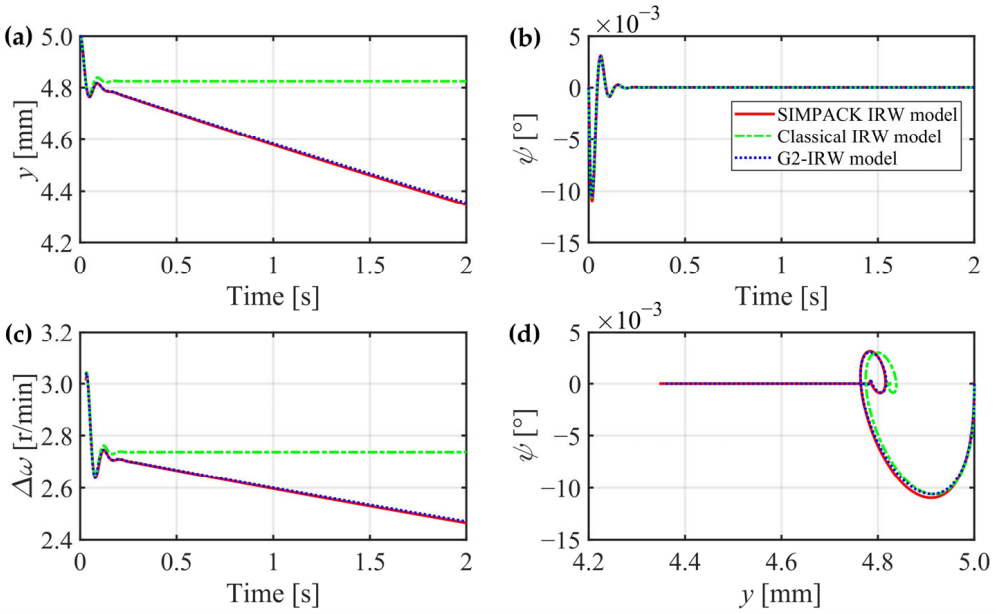

Figure 16. Lateral dynamics simulation results (V10-S10-C10). (**a**) Lateral displacement; (**b**) yaw angle; (**c**) differential wheel rotational speed; (**d**) $y - \psi$ phase diagram.

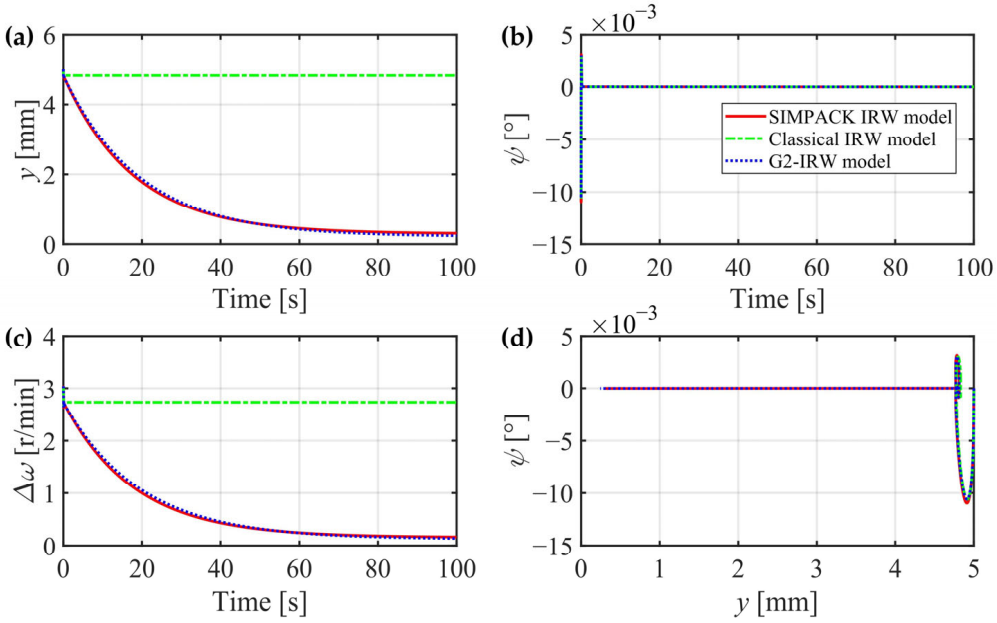

Figure 17. Lateral dynamics simulation results (V10-S10-C10, 100 s). (**a**) Lateral displacement; (**b**) yaw angle; (**c**) differential wheel rotational speed; (**d**) $y - \psi$ phase diagram.

Furthermore, the closeness between the G2-IRW model and the SIMPACK model indicates another accurate description of the IRW's dynamics for future study. Under consideration of cost, complexity, and real-time performance, only the rotational speeds of the wheels and the yaw angle of the IRW can be accurately measured. However, for better stability control and curve negotiation control of the IRW, the lateral displacement and the lateral velocity are key state variables that should be measured in real-time. Owing to the programmability and rapid iterative computability of the differential equations, Equations (28)–(31) is a better option for state observer design. Although irregularities input from the rail track and uncertain nonlinearity influences of the model coefficients exist in practice, according to the study on finite-time continuous extended state observers [22], the observer can be precisely designed and obtain excellent performance.

After verifying the G2-IRW model through comparison in simulations, the dynamic characteristics described by Equations (28)–(31) and the steady convergent process described by Equations (45)–(47) will be demonstrated and analyzed in the next section.

4. Dynamic Characteristics Analysis

As in the simulation results shown in Section 3, the dynamic characteristics of the IRW are highly affected by the gravitational restoring forces, the gyroscopic moment, and their interactions. Three types of dynamic motions can be observed through the comparisons under different conditions. They are derailment, hunting, and offset running. In addition, the dynamic motions change with the variations in velocity, yaw stiffness, and yaw damping. In this section, how these three factors' variations affect the dynamic motions of the IRW will be analyzed. The simulation results are totally from the G2-IRW model after comparisons with the one built in SIMPACK 2018 for precise and accurate descriptions. Consistent with Section 3, the initial step-input of all the simulations in Section 4 is also set as $y_0 = 0.005$ m.

4.1. The Three Types of Dynamic Motions

As Shown in Figure 18, if the IRW runs at 15 m/s and with no yaw suspension, the gravitational restoring moment plays an important role in the IRW's dynamics motion, resulting in derailment. If just a yaw damper is installed on the IRW, the derailment speed becomes slower. If just a yaw spring is installed on the IRW with a proper stiffness

coefficient, the gravitational restoring moment can be conquered. Then, under the effects of the gyroscopic moment, the hunting motion is generated. However, the mechanism of the hunting motion on the IRW differs from that on the SW, because the gyroscopic moment is much smaller than the longitudinal creep moment on the SW. Then, the self-guidance ability of the IRW is much lighter than that of the SW, and it is constrained by the yaw spring to some extent. Therefore, although the dynamic process presents as hunting motion, the long-time average lateral displacement presents as offset running. If both a yaw spring and a yaw damper are installed, the hunting motion can be suppressed. Then, the IRW can be suppressed into the steady convergent process and only presents as offset running. If the simulation duration is long enough, the lateral displacement can eventually converge to zero or nearly zero.

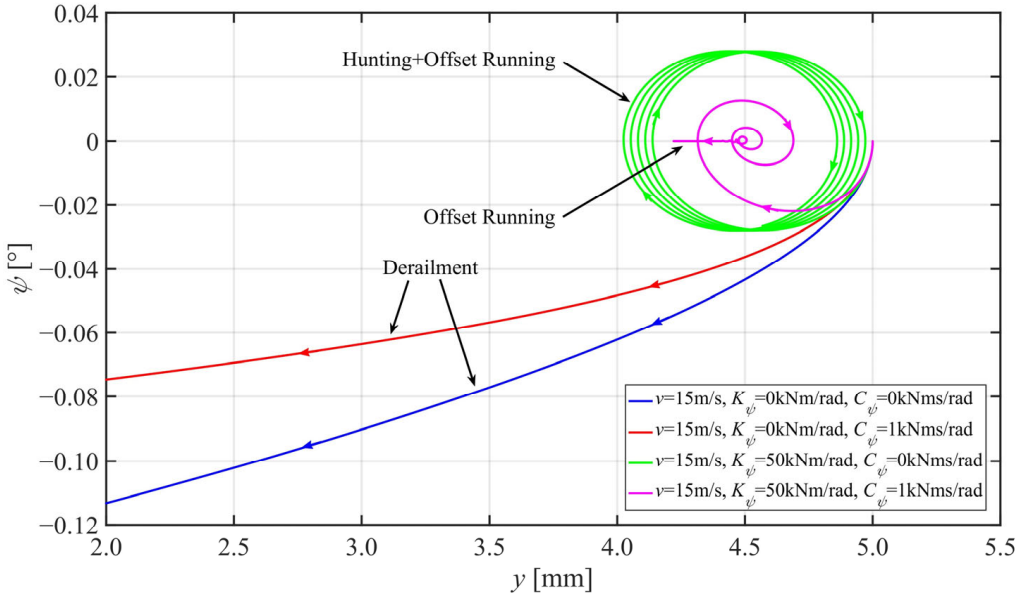

Figure 18. $y - \psi$ phase diagram ($v = 15$ m/s) with different yaw suspension configurations.

The blue curve in Figure 19 demonstrates that when the IRW runs at a high speed, the derailment tendency caused by the gravitational restoring moment can be conquered by the gyroscopic moment, and the IRW's motion presents as hunting. Furthermore, the long-time average lateral displacement is close to zero. This phenomenon proves that if the speed is high enough, the gyroscopic moment can recouple the two wheels of the IRW, and then the self-guidance ability is generated. If just a yaw damper is installed, the hunting motion is suppressed, and the IRW can run along the center of the straight rail track. If just a yaw spring is installed, the self-guidance ability of the IRW is constrained to some extent, and the IRW's motion presents as hunting with offset running. If both a yaw spring and a damper are installed, the hunting motion can be suppressed, and the IRW's motion enters the steady convergent process after damped oscillations.

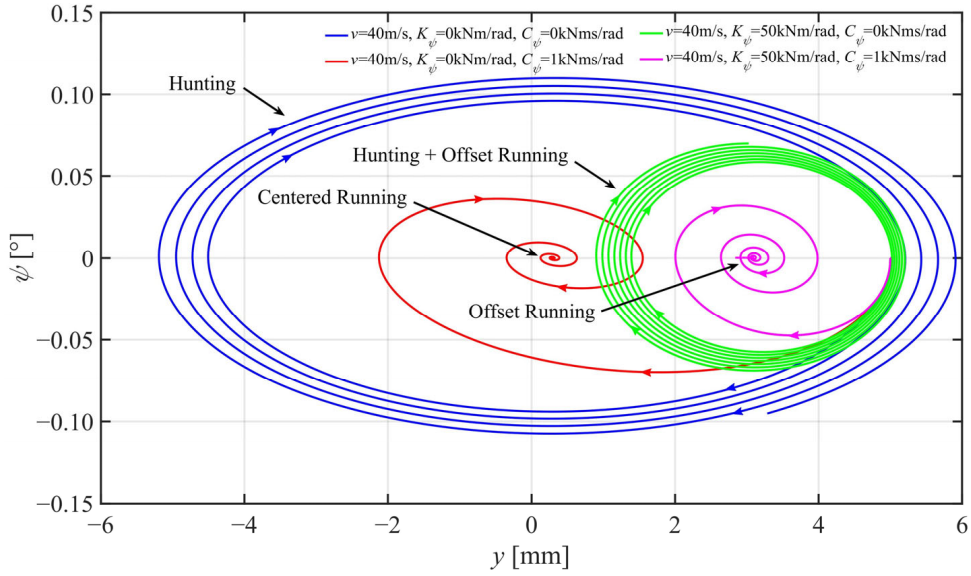

Figure 19. $y - \psi$ phase diagram ($v = 40$ m/s) with different yaw suspension configurations.

4.2. Steady Convergent Process

As shown in Figure 20, after entering the steady convergent process, the end states of all the curves from different initial states are located on a straight line in the three-dimensional space expanded by $y - \psi - \Delta\omega$, and this straight line is in the plane $\psi = 0$. This finding validates Equation (47) deduced in Section 2.5. The straight line in Figure 20 can be calculated through the linear fitting method, which is $\Delta\omega = 13.49y + 1.33 \times 10^{-9}$. According to Equation (47), the theoretical function of the straight line is $\Delta\omega = 12.5y$, and the relative error is 7.9%. Due to some nonlinear issues of the wheel–rail contact, the equivalent wheel–rail tread conicity is not always equal to the wheel geometry tread conicity 0.1 but varies with the lateral displacement. Thus, the simulation results are a little different from the theoretical functions.

Figure 21 shows the whole process with a simulation duration of 500 s from only one initial state. The first stage of the entire motion is the dynamic process. In this stage, the IRW moves from the initial state to another on the straight line in plane $\psi = 0$. Once the state converges to this straight line, the motion will enter the second stage, the steady convergent process. In this stage, the IRW converges to $(y = 0, \psi = 0, \Delta\omega = 0)$ along the straight line following the law depicted by Equation (47).

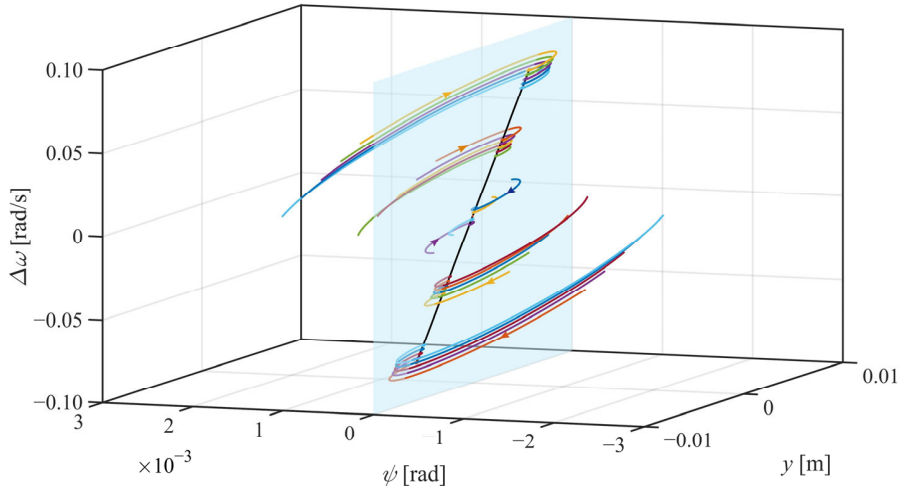

Figure 20. $y - \psi - \Delta\omega$ phase diagram ($v = 10$ m/s, $K_\psi = 10$ kNm/rad, $C_\psi = 1$ kNms/rad) from different initial states.

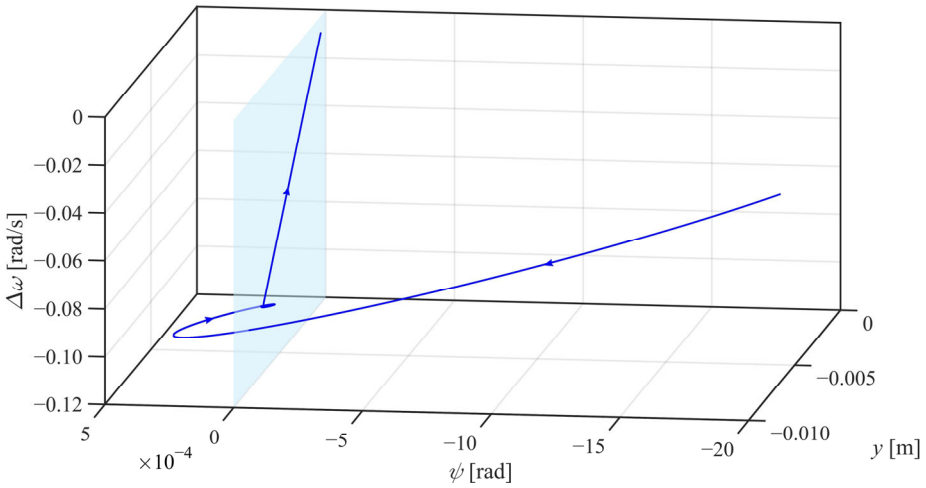

Figure 21. $y - \psi - \Delta\omega$ phase diagram ($v = 10$ m/s, $K_\psi = 10$ kNm/rad, $C_\psi = 1$ kNms/rad) from initial states ($y_0 = -0.005$, $\psi_0 = -0.002$ rad).

Under the interactions among the gravitational restoring forces, gyroscopic moment, and yaw suspension, the dynamics of the IRW are complicated, making the IRW technology hard to apply to urban railway vehicles. Three types of dynamic motions exist: derailment, hunting, and offset running. Only at high speed and with a yaw damper can the IRW run along the center of the rail track. Under other conditions, the dynamic motions of the IRW are unwanted in practical applications. In addition, with proper yaw suspension coefficients, IRW's state can converge to zero eventually, but the steady convergent process takes a long time, usually hundreds of seconds, which is unacceptable. Thus, self-guidance control is still essential for the IRW, especially at low speeds.

Although the dynamic characteristics and the steady convergent process are verified by simulation results, due to considerations of inevitable irregularities input from the rail track and time-varying nonlinear frictions generated by bearings, the experimental verification illustrated in the next section is strongly necessary.

5. Experimental Verification

For further study of the wheelset or bogie dynamics, the full-size or scaled roller rig technique is widely used in many research institutions and universities [8,13,17,19,23]. We built a 1/9 scaled IRW system to verify the existence of the three dynamic characteristics of the IRW mentioned in Section 4. We collected and recorded the experimental phenomena as presented in the Supplementary Materials Video S1.

As Shown in Figure 22c,d, the roller is driven by a large-torque electric motor, and the wheelset on the roller can be regarded as an IRW of a trailer truck. Figure 22b demonstrates that a pair of yaw suspensions are installed between the traction plate and the IRW. A thrust ball bearing is installed between the IRW and the traction plate, which makes the friction in the yaw direction negligible, so when disconnecting the yaw suspension, the IRW can yaw toward the traction plate freely. In the measurement system, two laser displacement sensors, one yaw angle sensor, and a pair of rotary encoders are installed, as shown in Figure 22a,b. Lateral displacement y, yaw angle ψ, and wheel rotational speeds ω_L and ω_R can be measured accurately, synchronously, and in real-time. With a rotary encoder installed on the roller's axle, the rotational speed of the roller can be stably controlled, varying from 0 to 300 r/min with a less than ± 1 r/min fluctuation. Correspondingly, the rotational speed of the wheels can vary from 0 to 2250 r/min.

As shown in Figure 23a, the two wheels are solid and adopt a 1/10 linear conicity tread with a 4 cm length of the linear section in width. The surface profile of the roller near the wheel–roller contact patches is shown in Figure 23b. The fundamental physical parameters of this scaled IRW are shown in Table 5.

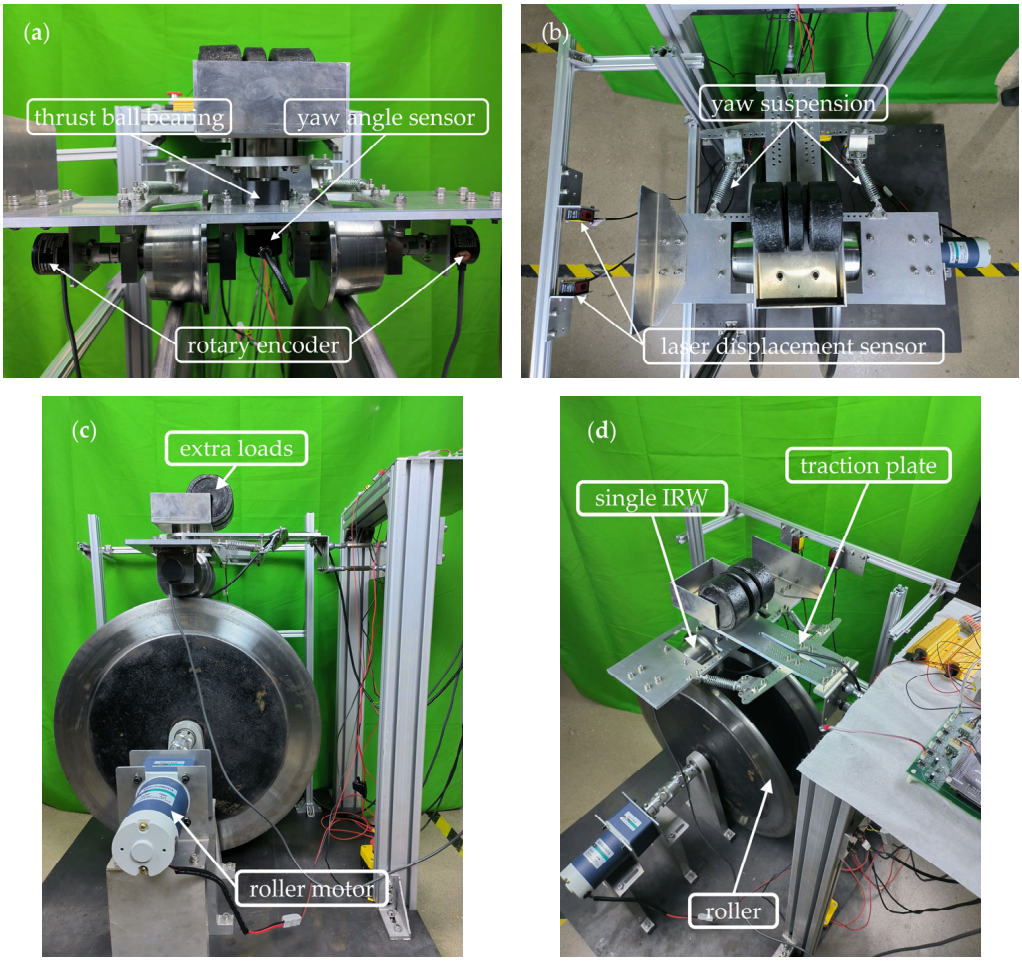

Figure 22. The scaled IRW experimental roller rig. (**a**) Back view; (**b**) top view; (**c**) side view; (**d**) oblique view.

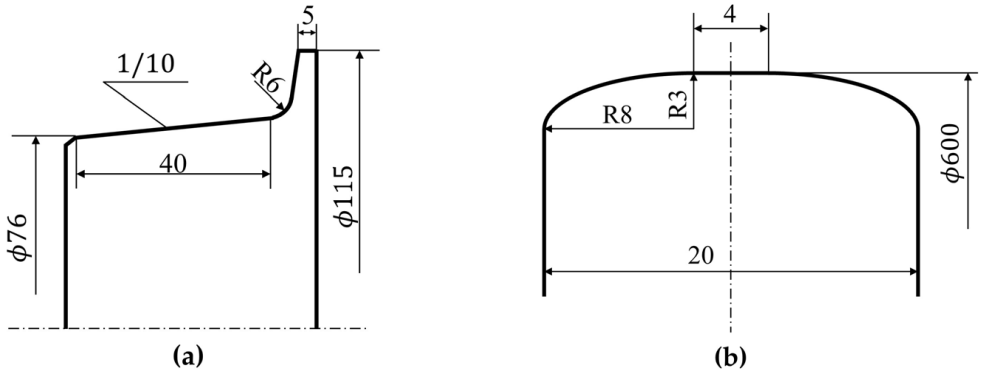

Figure 23. The profile design for the experiments. (**a**) Wheel tread; (**b**) roller surface.

Table 5. The scaled IRW's parameters in experiments.

Symbol	Definition	Value
m	Total mass of IRW	10.62 kg
m_W	Wheel mass	2.92 kg
J_{Cx}	Carrier's inertia moment in the x direction	5.53×10^{-2} kg·m^2
J_{Cy}	Carrier's inertia moment in the y direction	5.94×10^{-3} kg·m^2
J_{Cz}	Carrier's inertia moment in the z direction	5.32×10^{-2} kg·m^2

Table 5. *Cont.*

Symbol	Definition	Value
J_{Wx}	Wheel′s inertia moment in the x direction	3.08×10^{-3} kg·m^2
J_{Wy}	Wheel′s inertia moment in the y direction	3.91×10^{-3} kg·m^2
J_{Wz}	Wheel′s inertia moment in the z direction	3.08×10^{-3} kg·m^2
b	Half lateral distance between the left and right wheels	0.083 m
r_0	Nominal wheel radius	0.04 m
λ	Equivalent wheel–rail tread conicity at the center position	0.1
d_r	Nominal roller diameter	0.6 m
m_z	Extra vertical loads	5 kg

5.1. Derailment

The yaw suspensions of the scaled IRW can be disconnected, as shown in Figure 24. The experimental results in Figure 25 demonstrate that if the IRW rides at low speeds without any yaw suspension, the states of the IRW will all diverge, which means that the IRW will ride towards one side of the rail until the wheel flange contacts with the rail profile, and the IRW will not come back to the center of the rail track again. The derailment tendency caused by the gravitational restoring moment discussed in Section 2.2 is verified.

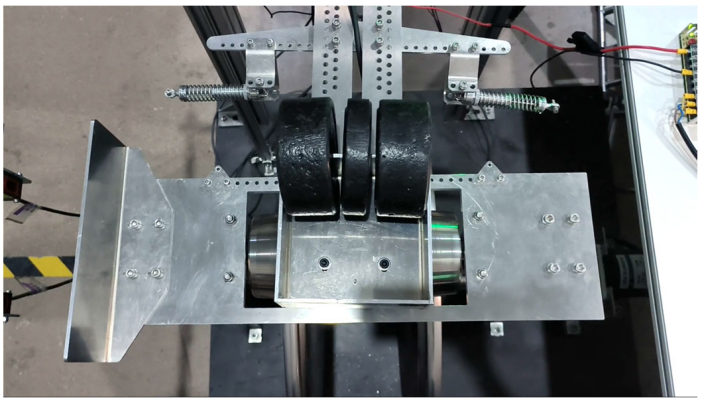

Figure 24. The scaled IRW without any yaw suspension.

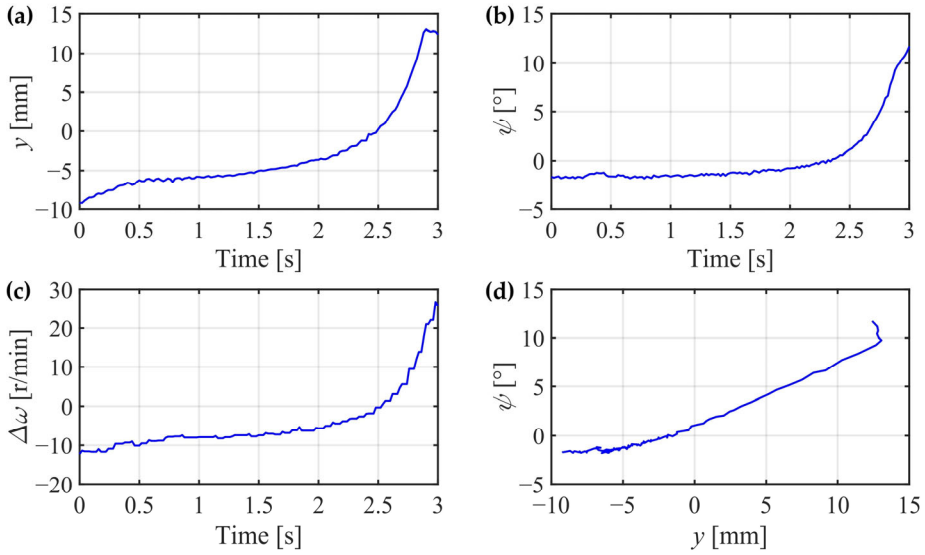

Figure 25. Experiment results of the IRW without any yaw suspension at average rotational speed 200 r/min. (**a**) Lateral displacement; (**b**) yaw angle; (**c**) differential wheel rotational speed; (**d**) $y - \psi$ phase diagram.

It is necessary to re-install the yaw suspensions onto the IRW and re-conduct the experiment at the same speed. All the states of the IRW converge, as shown in Figure 26, which shows the same dynamic characters as the simulation results in Section 4.1.

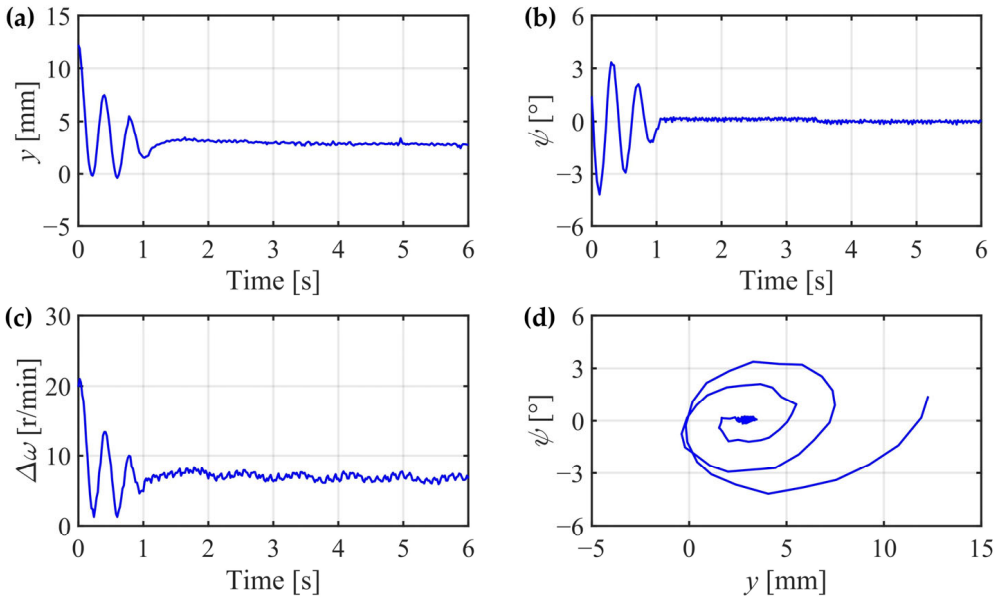

Figure 26. Experiment results of the IRW with yaw suspensions at average rotational speed 200 r/min. (**a**) Lateral displacement; (**b**) yaw angle; (**c**) differential wheel rotational speed; (**d**) $y - \psi$ phase diagram.

5.2. Hunting

If the yaw suspensions are all disconnected, and the IRW is accelerated to the wheel rotational speed of 895 r/min, a unique phenomenon similar to the hunting motion on the SW will also appear on the IRW, as shown in Figure 27. The experimental results show that the lateral displacement y and yaw angle ψ oscillate alternately. However, the differential wheel rotational speed $\Delta\omega$ also varies with y, which differs from the SW. This phenomenon demonstrates that although the IRW rides without any yaw suspension, if the rotational speeds of the wheels are high enough, the derailment tendency will be conquered, and the self-guidance ability will be regained. The experimental results are in accordance with the simulation results in Sections 3 and 4.1, and the phenomenon can be interpreted by the gyroscopic effects discussed in Section 2.3.

It is necessary to re-install the yaw suspensions and let the IRW still run at a high speed. The experimental results are shown in Figure 28. The critical oscillation velocity of the IRW with yaw suspensions is 800 r/min. It demonstrates a counterintuitive phenomenon that if yaw suspensions with relatively low yaw damping are installed, the critical oscillation velocity of the IRW is lower than that without yaw suspensions. Furthermore, the frequency of the oscillation is higher. It is analyzed that the function of the yaw spring on the IRW is not to suppress the oscillation but to resist the derailment tendency caused by the gravitational restoring moment. It is the yaw damper that is the main factor contributing to oscillation suppression. When the derailment tendency is resisted or partially resisted, the slight self-guidance effects caused by the gyroscopic moment dominate the lateral motion. Then, the oscillation is prone to appear. If the longitudinal speed decreases, the oscillation is suppressed by the yaw dampers, as shown in Figure 29. Due to the limitation of the suppression ability of the yaw dampers on the scaled IRW in this paper, the oscillation appears when the speed is high enough.

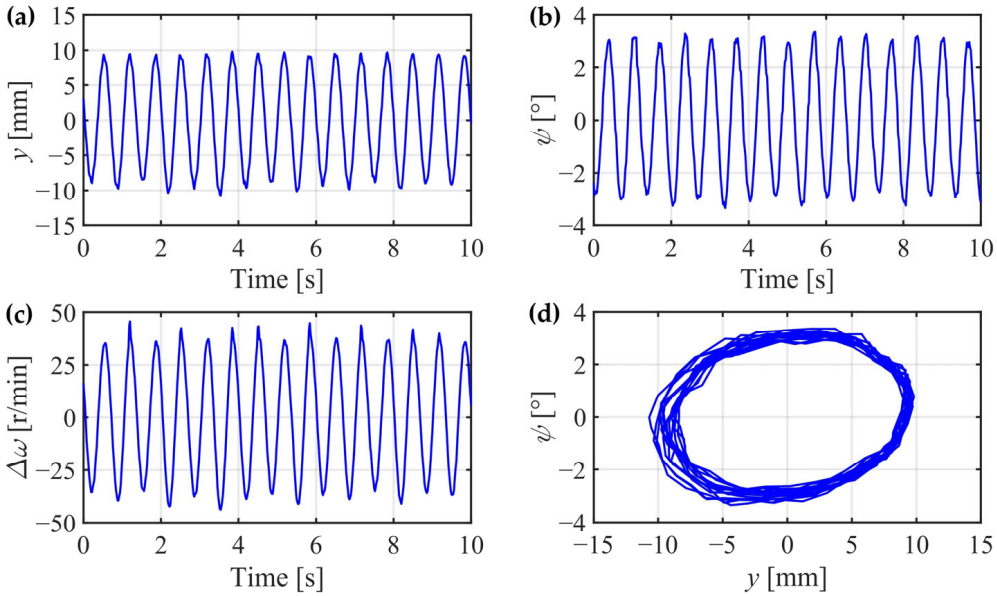

Figure 27. Experiment results of the IRW without any yaw suspension at average rotational speed 895 r/min. (**a**) Lateral displacement; (**b**) yaw angle; (**c**) differential wheel rotational speed; (**d**) $y - \psi$ phase diagram.

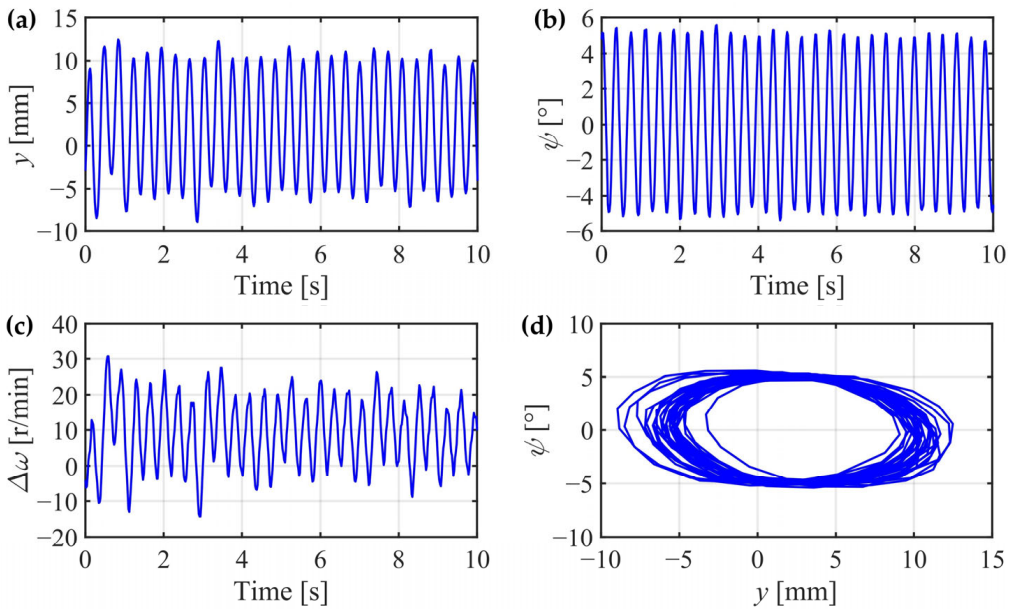

Figure 28. Experiment results of the IRW with yaw suspensions at average rotational speed 800 r/min. (**a**) Lateral displacement; (**b**) yaw angle; (**c**) differential wheel rotational speed; (**d**) $y - \psi$ phase diagram.

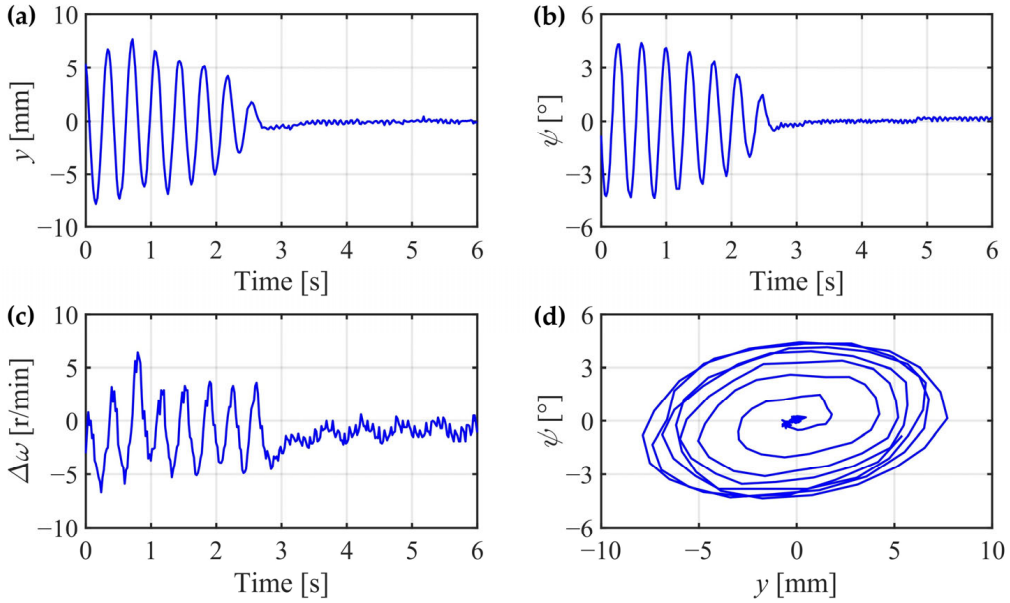

Figure 29. Experiment results of the IRW with yaw suspensions at average rotational speed 620 r/min. (**a**) Lateral displacement; (**b**) yaw angle; (**c**) differential wheel rotational speed; (**d**) $y - \psi$ phase diagram.

5.3. Offset Running

When the IRW enters the steady convergent process, the dynamic oscillations are suppressed by the yaw suspensions, and the IRW only presents offset running, as described by Equations (45)–(47) in Section 2.5. Here, we applied some instantaneous lateral disturbances in sequence on the traction plate. The process of each disturbance input is shown in Figure 30.

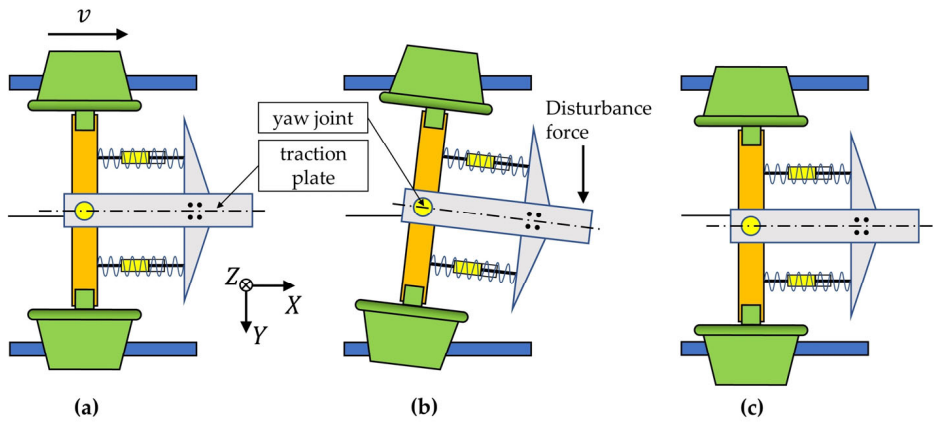

Figure 30. Apply instantaneous lateral disturbance force after the IRW enters the steady convergent process. (**a**) Before disturbance; (**b**) under disturbance; (**c**) after disturbance.

Considering the IRW being installed on an IRW bogie, the traction plate shown in Figures 22d and 30 can be regarded as the "bogie frame". When disturbance force is applied on the bogie frame, the bogie's heading angle will change, leading to yaw angle variations in the IRW. Because of the relation between the longitudinal creep forces and the yaw angular velocity $\dot{\psi}$ of the IRW in the wheel rotational direction, as demonstrated in Equations (30) and (31) in Section 2.4, the rotational angular accelerations of the two wheels, $\dot{\omega}_L$ and $\dot{\omega}_R$, will change. When the disturbance force is removed, because the longitudinal creep forces also relate to the lateral displacement y, the rotational speeds of the two wheels will continuously vary with y. The regulation law can be inferred as follows

$$\begin{cases} y\uparrow, \dot{\omega}_{\mathrm{L}} > 0, \dot{\omega}_{\mathrm{R}} < 0, \omega_{\mathrm{L}}\uparrow, \omega_{\mathrm{R}}\downarrow \\ y\downarrow, \dot{\omega}_{\mathrm{L}} < 0, \dot{\omega}_{\mathrm{R}} > 0, \omega_{\mathrm{L}}\downarrow, \omega_{\mathrm{R}}\uparrow \end{cases} \tag{49}$$

Then, the IRW will eventually reach another steady state with another $(y, \omega_{\mathrm{L}}, \omega_{\mathrm{R}})$.

As shown in Figure 31, several instantaneous lateral disturbances act on the IRW every 10 s. Because the disturbances are instantaneous and the longitudinal creep forces vary simultaneously, the whole stabilization process is too short to be detected in detail. The lateral displacement y and the differential wheel rotational speed $\Delta\omega$ both change after each disturbance, and almost remain unchanged during the intervals of the adjacent two disturbance inputs.

The yaw angle sensor is installed on the yaw joint shown in Figures 22a and 30, so only the yaw angle to the traction plate can be measured. Under the suppression effects of the yaw suspensions, the yaw angle to the traction plate is almost unchanged during the stabilization process of each disturbance. That is why the curve of ψ in Figure 31 stays around 0° just with the sensor noise during the 120 s experiment.

The average lateral displacement y and average differential wheel rotational speed $\Delta\omega$ can be calculated in every interval of the adjacent two disturbances. The linear regression results of these data points are demonstrated in Figure 32, which shows a positive linear relation between $\Delta\omega$ and y. According to Equation (47) in Section 2.5, the theoretical slope of this line is 301.1, which means that the relative error is 9.4%. These experimental results also demonstrate that the IRW should have many steady states, which shows the exact characteristic of the offset running. That is, after the oscillation has been suppressed, the states on the straight line described by Equation (47) all become steady states. They finally converge to 0, but the steady convergent process is too long in practice, which means they can be treated as steady states and lead to the IRW's offset running. These features are in accordance with the analysis in Section 2.5 and previous simulation results in Section 4.2. Actually, if the real equivalent wheel–rail tread conicity and nominal wheel radius of the experiment IRW can be estimated more precisely on the scaled roller, the calculated theoretical slope is possibly more accurate.

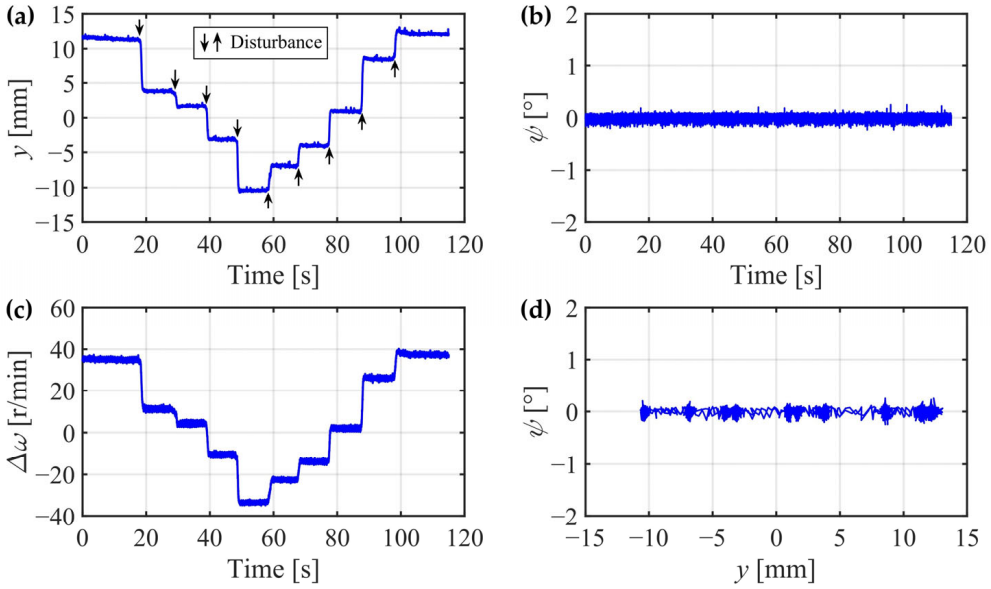

Figure 31. Experiment results of the IRW with yaw suspension at average rotational speed 575 r/min with disturbance inputs several times. (**a**) Lateral displacement; (**b**) yaw angle; (**c**) differential wheel rotational speed; (**d**) $y - \psi$ phase diagram.

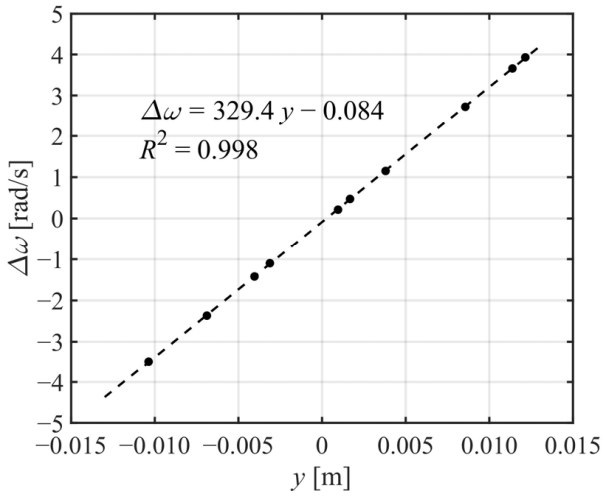

Figure 32. Linear regression results of the experiment data during IRW's offset running at average rotational speed 575 r/min.

6. Discussion

6.1. Initial State Selection

Although the initial states were not forced to a fixed point during the experimental verification, the three types of the IRW's dynamic characteristics, derailment, hunting, and offset running, are still observable and recognizable. During about half a year of conducting simulations and experiments, we have not encountered a situation where initial state selections can change the type of the dynamic characteristics. For example, the dynamic characteristic is always derailment if the IRW runs at low speeds and without yaw suspensions, no matter where the initial states are. In contrast, the dynamic characteristic is always offset running if the IRW runs at low speeds but with yaw suspensions, no matter where the initial states are. We found that for an already designed IRW system, only velocity, yaw stiffness, and yaw damping could significantly influence the type of the dynamic characteristics in one specific experiment. We speculate these three parameters prominently affect the system poles of the IRW's root locus diagrams and are now working on theoretical proof.

In view of the simulation results in Figure 20 and the analysis in Section 4.2, if proper yaw suspensions are deployed, no matter where the initial states are, the IRW will experience two stages: a damped dynamic stage and a steady convergent stage. Firstly, they all converge to the straight line described by Equation (47), as shown in Figure 20. Then, they will move slowly along this straight line to the origin ($y = 0, \psi = 0, \Delta\omega = 0$). This is a reflection of the simulation results on the explanation and speculation above.

Additionally, since the sensors are high-precision and sensitive, especially the roller continuously rotating during the whole experiment, it is difficult to ensure that we can put the scaled IRW precisely on one fixed-state point every time we begin to record results.

6.2. Precision Issues

Machining tolerances and bearing frictions are the two potential precision issues affecting the experimental results the most.

The larger the machine part is, the harder to guarantee the machining accuracy. The largest machine part of the scaled IRW experimental system is the roller, which also can input irregularity excitations on the IRW's wheels and affect the dynamic processes. Thus, the machining tolerances of the roller, especially of the surface profile near the wheel–roller contact patches, should be reduced. We collaborated with a machining company to build the experimental system. They have a large CNC lathe capable of machining a cylinder up to 60 cm in diameter, with a machining process accuracy of ± 0.01 mm. The geometry information of the surface profile was coded into the CNC lathe so the nonlinear

surface profile could be well processed. We used a dial gauge to check several points of the surface profile to check the machining tolerances, as shown in Figure 33. Because of the nonuniformity of materials, the roller will slightly deform with time. When the heavy scaled IRW with vertical loads runs on the roller, it will also slightly deform. In addition, the assembling clearances in the whole mechanical system deteriorate the machining working accuracy. Overall, the machining tolerances cannot be decreased to ±0.01 mm. We have made three versions of the experimental systems and can guarantee the machining tolerances within ±0.1 mm of the best one.

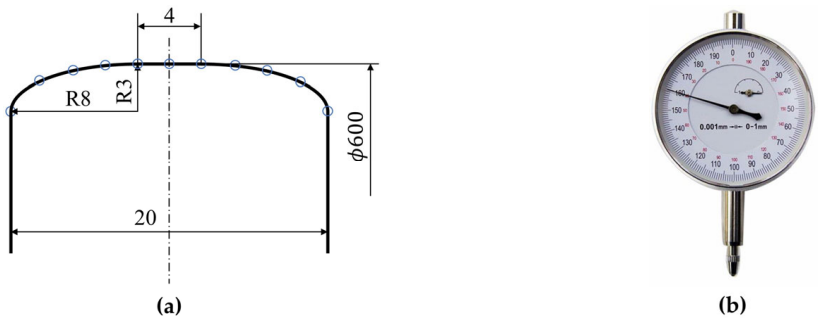

Figure 33. The machining tolerance test of the roller's surface profile near the wheel–roller contact patches. (**a**) The test points; (**b**) a dial gauge for checking the machining tolerances.

The three most important points for decreasing bearing frictions are guaranteeing installation accuracy, adopting high-quality bearings, and lubricating bearings before experiments. The carrier plate was processed in a CNC drilling and milling machine with a machining process accuracy of ±0.01 mm. The thread holes can be located accurately to guarantee installation accuracy. As shown in Figure 34, there are two types of relative rotations on the scaled IRW. One is the wheels' rotational motion to the carrier, and the other is the IRW's yaw motion to the traction plate. The ball bearings and thrust bearing were bought from an online professional machine parts supplier, MiSUMi, to reduce rotational frictions. The bearings' accuracy satisfied the Japanese standard JIS B 1514 Class 0 [24], meaning the rotational frictions of the bearings themselves are small enough. Moreover, we lubricated these bearings before experiments to decrease the bearing frictions.

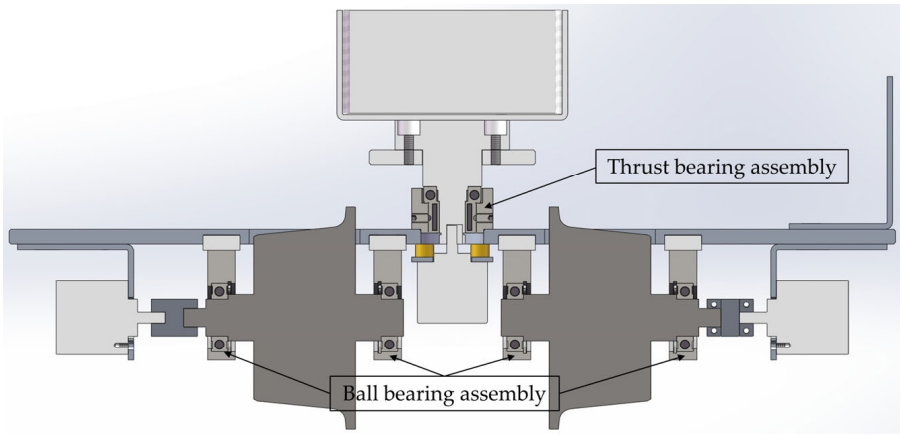

Figure 34. Bearings' installation on the scaled IRW.

Due to machining precision issues and the unavoidable bearing frictions, it is not reasonable to compare the experimental results of the scaled IRW with the one built in SIMPACK 2018 point by point in the time domain. Although we have made three sets of the experimental systems and chose the best one, the least machining tolerance of the roller is ±0.1 mm, which can still cause unwanted irregularity input and influence the results. As shown in Figures 26 and 29, the high-frequency oscillations in the steady convergent process demon-

strate the impact. The amplitude of the high-frequency oscillations on the differential rotational speed curve in Figure 29 is about 0.5 r/min. According to Equation (47), the corresponding lateral displacement y is 0.162 mm, which is very close to the machining tolerances of the roller.

However, the demonstrations of the three types of dynamic motions and the steady convergent process are not affected. The derailment, hunting, and offset running are still observable and recognizable. The experimental results are still in accordance with the theoretical analysis and the phenomena found in simulations.

6.3. Center of Gravity Position

Although no parameters directly indicate the center of gravity position in the lateral direction in the differential equations of the IRW's dynamics, the center of gravity position can affect the vertical loads on the wheels of each side, and then the Kalker's creep coefficients k_{11} and k_{22} of the two wheels will be different. In addition, if the mass distribution changes, the principal axis of inertia will change, and the inertia moments to the geometric rotation center will change. These variations will probably affect the dynamic process.

We changed the lateral position of the extra mass loads in the container, as shown in Figure 35, and conducted some experiments. Let y_{ec} denote the lateral position of the extra mass loads' gravity center to the axis of symmetry. The range of y_{ec} for adjustment is from -4 cm to 4 cm.

We found that the three dynamics characteristics still existed and could be observed. However, the critical speed ω_c between the offset running and hunting motion significantly varied with y_{ec}, as shown in Figure 36.

The faster the critical speed, the less potential to generate a hunting motion. The results shown in Figure 36 demonstrate that when $y_{ec} = 0$, the scaled IRW is most susceptible to the gyroscopic effects, and the hunting motion can be sustained at rotational speeds higher than 800 r/min. When $|y_{ec}| = 4$, according to the equation of gyroscopic moment described as Equation (16) in Section 2.3, a larger gyroscopic moment is needed to cause the hunting motion, meaning the scaled IRW is less prone to oscillate below the critical speed.

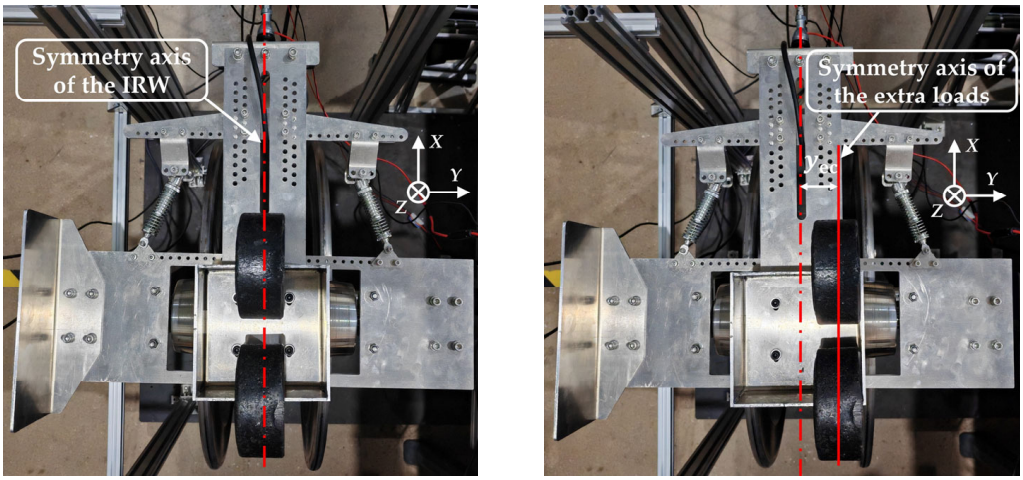

(**a**) (**b**)

Figure 35. The center of gravity position of the extra loads in the lateral direction. (**a**) Centered; (**b**) off-center.

Additionally, the effect of the gravity center's lateral position on the critical speed is nonlinear. We speculated that it is related to the interaction between the variations in the inertia moments and the variations in Kalker's creep coefficients. With the extra loads' gravity center becoming far from the axis of symmetry in the lateral direction, the inertia moments to the geometric rotation center grow larger, which makes the scaled IRW less prone to oscillate. However, the difference between the vertical loads on the two wheels also becomes larger, which decreases the average Kalker's creep coefficients and makes the scaled IRW more likely

to oscillate. The farther the gravity center's lateral position away from the axis of symmetry, the more significantly the dynamics are affected by the variation in Kalker's creep coefficients. These two factors cause the nonlinear variations in ω_c with y_{ec}. Nonetheless, more detailed experiments and theoretical analysis are needed for solid confirmation.

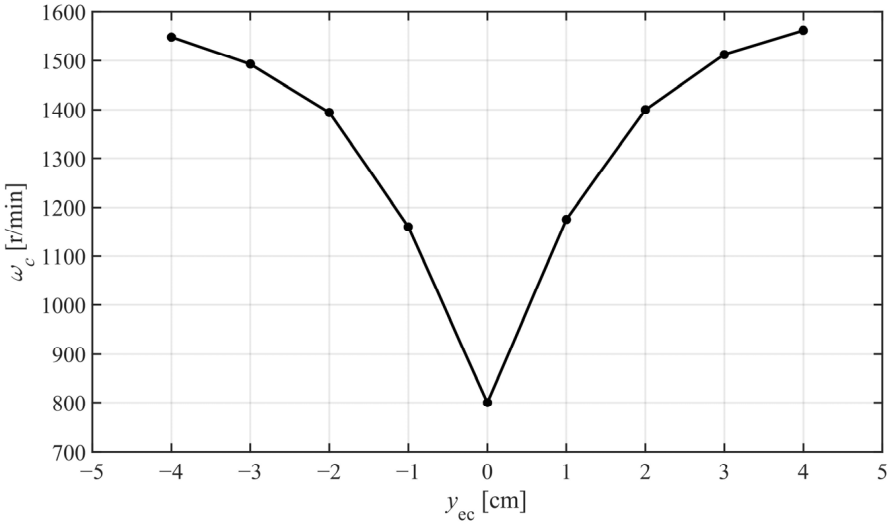

Figure 36. The experimental results of the critical speed ω_c with variations in y_{ec}.

Although the center of gravity position in the lateral direction can affect the dynamics process according to the experimental results, the steady states of the IRW can still be described by Equation (47) in Section 2.5. Because only the geometric parameters λ and r_0, and the longitudinal speed v can influence the equation, the relation between $\Delta\omega$ and y is not affected by the center of gravity position in the lateral direction.

6.4. Future Works

Although the three types of IRW's dynamics characteristics, derailment, hunting, and offset running, have been observed and presented during experiments, some potential areas are worthy of further exploration, listed as follows:

- The critical speed between the convergent process and the hunting motion needs to be determined theoretically or technically. It affects the security boundary in practice;
- Rail profile irregularities are prevailing and inevitable in practice. Whether the dynamic characteristics can be significantly affected needs to be verified on a real-life rail track;
- Only 1/10 linear conicity tread wheels are adopted in the present study. If nonlinear tread wheels were adopted, as shown in Figure 37, the dynamics would become more complicated and diversified;
- In view of the IRW's complex dynamics, how to design a reliable bogie structure and robust control methods to conquer the derailment, hunting, and offset running at different longitudinal speeds and how to realize a stabilized centered running state urgently need to be explored.

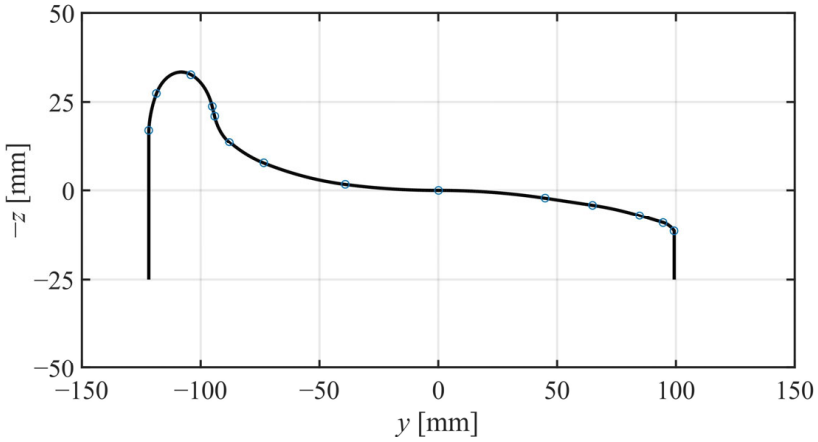

Figure 37. LM_A nonlinear wheel tread profile in the Chinese railway standard TB/T 449−2003 [25].

7. Conclusions

This paper reports on basic research investigating the dynamic characteristics of the IRW and its underlying mechanisms. Compared to the previous research, the creepages and creep forces are calculated separately on the wheels of each side. More importantly, the effects of the gravitational restoring forces and the gyroscopic moment are carefully considered and analyzed. An improved IRW model G2-IRW is derived through the Euler–Lagrange theorem, from which the three dynamic characteristics of the IRW, derailment, hunting, and offset running, are discovered and summarized. Simulations and scaled-model experiments verified the existence.

For an IRW without any yaw suspension, the gravitational restoring moment leads to derailment at low speeds, and the gyroscopic moment contributes to slight self-guidance ability at high speeds. When yaw suspensions are installed, the yaw spring can effectively prevent derailment at low speeds, and the yaw damper can effectively suppress hunting motion at high speeds. However, because the self-guidance ability is relatively slight, the IRW could stay in the offset running state for a long time. The mathematical steady-states analysis demonstrates negative-exponential convergence effects under the act of the gravitational restoring forces and an intrinsic linear relation of the IRW between the lateral displacement and the differential rotational speed.

The improved mathematical model of the IRW proposed in this paper was built in Simulink, and a model built in SIMPACK 2018 with the same set of model parameters was generated. The simulation results demonstrated that the improved mathematical model G2-IRW is much closer to the SIMPACK model than the classical one. In addition, a scaled roller rig and a scaled IRW were designed and built. All three dynamic characteristics: derailment, hunting and offset running, as well as the intrinsic relation law between the lateral displacement and the differential wheel rotational speed, appeared in the experimental results, through which the validity of the theoretical analysis is verified.

Supplementary Materials: The following supporting information can be viewed at: https://www.youtube.com/watch?v=zikUywBYqPg or https://www.bilibili.com/video/BV1fK411b7Ga/, (accessed on 20 December 2023). Video S1: Dynamic characteristics of the IRW for railway vehicles.

Author Contributions: Conceptualization, X.J.; methodology, X.J., Y.Y.; software, X.J.; validation, X.J., Y.Y.; formal analysis, X.J.; investigation, X.J.; resources, X.J. and W.W.; data curation, X.J.; writing—original draft preparation, X.J.; writing—review and editing, X.J., Y.Y. and W.W.; visualization, X.J. and Y.Y.; supervision, W.W.; project administration, W.W.; funding acquisition, W.W. All authors have read and agreed to the published version of the manuscript.

Funding: This research was funded by the National Natural Science Foundation of China, grant number 51575294.

Institutional Review Board Statement: Not applicable.

Informed Consent Statement: Not applicable.

Data Availability Statement: Data are contained within the article and Supplementary Materials.

Conflicts of Interest: The authors declare no conflicts of interest.

Abbreviations

IRW (independently rotating wheelset), SW (solid wheelset), DOF (degrees of freedom).

References

1. Satou, E.; Miyamoto, M. Dynamics of a bogie with independently rotating wheels. *Veh. Syst. Dyn.* **1992**, *20*, 519–534. [CrossRef]
2. Dukkipati, R.; Narayana Swamy, S.; Osman, M. Independently rotating wheel systems for railway vehicles-a state of the art review. *Veh. Syst. Dyn.* **1992**, *21*, 297–330. [CrossRef]
3. Heckmann, A.; Keck, A.; Grether, G. Active guidance of a railway running gear with independently rotating wheels. In Proceedings of the 2020 IEEE Vehicle Power and Propulsion Conference (VPPC), Gijon, Spain, 18 November–16 December 2020; pp. 1–5.
4. Eickhoff, B. The application of independently rotating wheels to railway vehicles. *Proc. Inst. Mech. Eng. Part F-J. Rail Rapid Transit* **1991**, *205*, 43–54. [CrossRef]
5. Cho, Y.; Kwak, J. Development of a new analytical model for a railway vehicle equipped with independently rotating wheels. *Int. J. Automot. Technol.* **2012**, *13*, 1047–1056. [CrossRef]
6. Goodall, R. Active railway suspensions: Implementation status and technological trends. *Veh. Syst. Dyn.* **1997**, *28*, 87–117. [CrossRef]
7. Perez, J.; Busturia, J.M.; Mei, T.; Vinolas, J. Combined active steering and traction for mechatronic bogie vehicles with independently rotating wheels. *Annu. Rev. Control* **2004**, *28*, 207–217. [CrossRef]
8. Michitsuji, Y.; Mizuno, K.; Suda, Y.; Lin, S.; Makishima, S. Curving performance evaluation of EEF bogie with inclined wheel axles using scale model vehicle. In Proceedings of the Advances in Dynamics of Vehicles on Roads and Tracks: Proceedings of the 26th Symposium of the International Association of Vehicle System Dynamics, IAVSD 2019, Gothenburg, Sweden, 12–16 August 2019; pp. 537–540.
9. Ji, Y.; Huang, Y.; Leng, H.; Ren, L.; Zhou, J.; Gong, D. Dynamic characteristics and friction torque design method for bogies with friction coupling independently rotating wheelsets. *Veh. Syst. Dyn.* **2022**, *60*, 1461–1487. [CrossRef]
10. Suda, Y. Improvement of high speed stability and curving performance by parameter control of trucks for rail vehicles considering independently rotating wheelsets and unsymmetric structure. *JSME Int. J. Ser. III* **1990**, *33*, 176–182. [CrossRef]
11. Mei, T.; Goodall, R.M. Robust control for independently rotating wheelsets on a railway vehicle using practical sensors. *IEEE Trans. Control Syst. Technol.* **2001**, *9*, 599–607. [CrossRef]
12. Mei, T.; Goodall, R. Practical strategies for controlling railway wheelsets independently rotating wheels. *J. Dyn. Syst. Meas. Control-Trans. ASME* **2003**, *125*, 354–360. [CrossRef]
13. Suda, Y.; Wang, W.; Nishina, M.; Lin, S.; Michitsuji, Y. Self-steering ability of the proposed new concept of independently rotating wheels using inverse tread conicity. *Veh. Syst. Dyn.* **2012**, *50*, 291–302. [CrossRef]
14. Liu, X.; Goodall, R.; Iwnicki, S. Yaw compensation and yaw relaxation controls for active steering of railway wheelsets via electromechanical actuators. *Proc. Inst. Mech. Eng. Part F-J. Rail Rapid Transit* **2022**, *236*, 70–79. [CrossRef]
15. Goodall, R.; Li, H. Solid axle and independently-rotating railway wheelsets-a control engineering assessment of stability. *Veh. Syst. Dyn.* **2000**, *33*, 57–67. [CrossRef]
16. Sugiyama, H.; Matsumura, R.; Suda, Y.; Ezaki, H. Dynamics of Independently Rotating Wheel System in the Analysis of Multibody Railroad Vehicles. *J. Comput. Nonlinear Dyn.* **2011**, *6*, 011007. [CrossRef]
17. Liang, B.; Iwnicki, S. Independently rotating wheels with induction motors for high-speed trains. *J. Control Sci. Eng.* **2011**, *2011*, 1–7. [CrossRef]
18. Ji, Y.; Ren, L.; Zhou, J. Boundary conditions of active steering control of independent rotating wheelset based on hub motor and wheel rotating speed difference feedback. *Veh. Syst. Dyn.* **2018**, *56*, 1883–1898. [CrossRef]
19. Yang, C.; Xu, N.; Wang, W.; Li, W.; Ren, Z. Self-steering performance of a new bogie with four independently rotating wheels using caster angle. *Int. J. Rail Transp.* **2023**, 1–16. [CrossRef]
20. Kurzeck, B.; Heckmann, A.; Wesseler, C.; Rapp, M. Mechatronic track guidance on disturbed track: The trade-off between actuator performance and wheel wear. *Veh. Syst. Dyn.* **2014**, *52*, 109–124. [CrossRef]
21. Kalker, J. Wheel-rail rolling contact theory. *Wear* **1991**, *144*, 243–261. [CrossRef]
22. Razmjooei, H.; Palli, G.; Abdi, E.; Strano, S.; Terzo, M. Finite-time continuous extended state observers: Design and experimental validation on electro-hydraulic systems. *Mechatronics* **2022**, *85*, 102812. [CrossRef]
23. Jaschinski, A.; Chollet, H.; Iwnicki, S.; Wickens, A.; Würzen, J. The application of roller rigs to railway vehicle dynamics. *Veh. Syst. Dyn.* **1999**, *31*, 345–392. [CrossRef]

24. *JIS B 1514*; Rolling Bearings—Geometrical Product Specifications (GPS) and Tolerance Values. The Japan Bearing Industry Association (JBIA): Tokyo, Japan, 2017.
25. *TB/T 449−2003*; Wheel Profile for Locomotive and Car. Ministry of Railways of the People's Republic of China: Beijing, China, 2003.